POLITECNICO DI TORINO
Repository ISTITUZIONALE

Numerical and experimental predictions of the static behaviour of thick sandwich beams using a mixed {3,2}-RZT formulation

Original
Numerical and experimental predictions of the static behaviour of thick sandwich beams using a mixed {3,2}-RZT formulation / Sorrenti, M., Gherlone, M.. - In: FINITE ELEMENTS IN ANALYSIS AND DESIGN. - ISSN 0168-874X. - ELETTRONICO. - 242:(2024). [10.1016/j.finel.2024.104267]

Availability:
This version is available at: 11583/2993150 since: 2024-10-08T08:09:54Z

Publisher:
Elsevier

Published
DOI:10.1016/j.finel.2024.104267

Terms of use:

This article is made available under terms and conditions as specified in the corresponding bibliographic description in the repository

Publisher copyright

(Article begins on next page)

06 June 2026

Finite Elements in Analysis and Design 242 (2024) 104267

Contents lists available at ScienceDirect

Finite Elements in Analysis & Design

journal homepage: www.elsevier.com/locate/finel

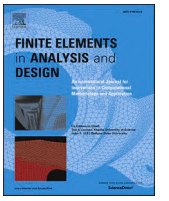

Numerical and experimental predictions of the static behaviour of thick sandwich beams using a mixed {3,2}-RZT formulation

M. Sorrenti *, M. Gherlone

Department of Mechanical and Aerospace Engineering – Politecnico di Torino, Corso Duca degli Abruzzi 24, 10129, Torino, Italy

ARTICLE INFO

Keywords:
Sandwich beams
Three-point bending
Four-point bending
Transverse deformability
Mixed {3,2}-RZT elements
Foam core
Distributed fibre optic sensors

ABSTRACT

This paper presents a numerical and experimental assessment of the static behaviour of thick sandwich beams using the mixed {3,2}-Refined Zigzag Theory ($RZT^{(m)}_{\{3,2\}}$). The displacement field of the $RZT^{(m)}_{\{3,2\}}$ assumes a piecewise continuous cubic zigzag distribution for the axial contribution and a smoothed parabolic variation for the transverse one. At the same time, the out-of-plane stresses are assumed continuous a-priori: the transverse normal stress is given as a third-order power series expansion of the thickness coordinate, whereas the transverse shear one is derived through the integration of Cauchy's equation. The equilibrium equations and consistent boundary conditions are derived through a mixed variational statement based on the Hellinger-Reissner (HR) theorem and a penalty functional to enforce the strain compatibilities between the assumed independent stress fields and those obtained with the constitutive equations. Based on the proposed model, a simple C^0-continuous two-node beam finite element is formulated (2B – $RZT^{(m)}_{\{3,2\}}$). Firstly, the analytical and FE model accuracies of the presented formulation are addressed, and comparisons with the available three-dimensional elasticity solutions are performed. Subsequently, an experimental campaign is conducted to evaluate the static response of various thick sandwich beam specimens in three- and four-point bending configurations. The thick beam specimens are equipped with Distributed Fibre Optic Sensors (DFOS) embedded in the sandwich layup to measure axial deformation at the sandwich interfaces directly. Finally, the experimental data are compared with the available numerical models, highlighting the formulated numerical model's performances and limitations.

1. Introduction

Sandwich structures are frequently used in many engineering fields, such as aerospace, naval, civil and energy applications. They typically consist of two stiff face-sheets (usually made of metallic laminates or multilayered composite) and a low-density thick core, such as honeycombs, foams, auxetics or lattices. This particular layup configuration leads to an improvement of the mechanical stiffness properties of its constituent materials, maintaining at the same time a reduced weight. Moreover, the recent advancements in the sandwich manufacturing processes [1] enable a new generation of high-performance and customised sandwich structures. However, the material heterogeneity intrinsically present along the transverse direction influences the mechanical response, and if not adequately predicted, it could lead to catastrophic failures such as core ruptures and face wrinkles/indentation [2]. It is, therefore,

* Corresponding author.
E-mail address: matteo.sorrenti@polito.it (M. Sorrenti).

https://doi.org/10.1016/j.finel.2024.104267
Received 4 July 2024; Received in revised form 23 September 2024; Accepted 29 September 2024
Available online 7 October 2024
0168-874X/© 2024 The Authors. Published by Elsevier B.V. This is an open access article under the CC BY license (http://creativecommons.org/licenses/by/4.0/).

clear the need to correctly predict the complex sandwich behaviour, by providing computational affordable and accurate numerical tools.

From a numerical point of view, sandwich structures have been widely investigated in the past years. Various researchers were able to provide the exact solution to the three-dimensional elasticity problems for sandwich structures. However, these are limited to simple configuration schemes and very specific load cases. For instance, among them are worthy to be cited the works of Pagano [3,4], Burton and Noor [5] and Brischetto [6]. Due to the difficulty in reaching the exact analytical solution, an alternative is represented by high-fidelity three-dimensional Finite Element (FE) models that can be adapted to a wide range of geometries and load configurations. On the other hand, if the number of degrees of freedom rapidly increases, the computational cost becomes prohibitive, especially when a more refined modelisation is required to describe a more complicated core geometry. As a matter of fact, a common procedure adopted by engineers is to assume the complex core structure behaviour as an equivalent homogeneous isotropic/orthotropic material whose properties can be determined using ad-hoc procedures [7–10].

Thanks to the homogenisation approaches, a sandwich structure can be easily analysed using the most famous displacement-based theories available in the current literature. Depending on the sandwich beam geometry and/or lamination scheme, the Equivalent Single Layer (ESL) or the Layer-Wise (LW) theories can be more/less suitable to predict accurately the structural response at a competitive computational cost. The formers assume a displacement field described by few kinematic variables valid for the whole laminate. This assumption guarantees a general accuracy on the global structural response (such as maximum displacements, critical loads and fundamental frequency) and computational attractiveness. However, they are often unable to be accurate in strain/stress predictions. On the other hand, the LW models, thanks to their displacement field description, which is assumed independently for each layer, are generally more accurate than the ESL ones, but for lamination schemes with several layers, these models are significantly more expensive in terms of computer resources. Among the ESL and LW models, in the sandwich framework, the Higher-order SAndwich Panel Theory (HSAPT) introduced by Frostig et al. [11,12] can be seen as an alternative and relatively simple theory. It assumes that the Bernoulli-Euler beam model describes the kinematics of both face-sheets, whereas the core layer carries the transverse shear and transverse normal deformability. The interested reader can find a more detailed overview of ESL, LW models and other theories for sandwich applications in Birman and Kardomateas's review [13].

In recent decades, the ZigZag Theories (ZZTs) have been widely adopted to address simple and complex sandwich problems. In ZZTs, the displacement field is composed of two main contributions: the first one can reproduce the global laminate behaviour, similarly to the ESL theories; the second one is a local refinement of the in-plane displacements, represented by appropriate zigzag functions characterised by the satisfaction of the transverse shear stress continuity at the layer interfaces. Starting from the pioneering works by Di Sciuva [14], whose zigzag functions ensured the full transverse shear stress continuity, other researchers have developed various ZZTs by choosing how to describe the in-plane contribution differently (see, for instance, Cho and Parmerter [15], Loredo et al. [16], Icardi [17]). Within this context, the Refined Zigzag Theory (RZT), introduced by Tessler et al. [18] to overcome some limitations on Di Sciuva's ZZT, has been demonstrated to accurately describe the response of sandwich structures, as reported in Refs. [19,20]. The remarkable accuracy and computational advantages (e.g. C^0-continuity requirement for FE formulations) offered by the RZT formulation in analysing multilayered composite and sandwich structures is testified by the variety of works currently available in the literature. For instance, Hasim and co-workers have applied the RZT model in conjunction with the Iso-Geometric Analysis [21–23] for analysing multilayered beams and plate structures; the RZT has been used to investigate the delamination effects in composite laminated beams by Groh et al. [24] and Eijo et al. [25]; an experimental-numerical comparison using the RZT to predict the fracture beahviour of glass/carbon fiber hybrid composites has been reported in Tabrizi et al. [26]; the RZT has been combined with the Peridynamic Differential Operator to determine the response of imperfect functionally graded porous sandwich beams [27]; for the first time, Truong et al. [28] combined the RZT with a neural network algorithm to improve the static analysis of laminated composite plates. More recently, the RZT has been applied in conjunction with the inverse-Finite Element Method (iFEM) for Structural Health Monitoring of composites and sandwich structures in Refs. [29–31], highlighting the robustness of the model even for shape-sensing applications. In addition to the linear formulations, higher-order RZT ones have been developed to address cases in which the displacement non-linearities are more pronounced, such as thick structures. As an example, in Ref. [32], the in-plane and transverse displacement components have been enriched with parabolic higher-order terms for the free and forced vibration of laminated plates. In Yurtsever et al. [33] the RZT formulation takes into account only the transverse stretching effect in the laminated composite beams, through a quadratic through-the-thickness variation of the transverse displacement component. The accuracy in predicting the structural behaviour for thick sandwich structures using the RZT kinematics has been investigated using mixed variational formulations, in which the displacement and transverse stress fields are assumed independently. For instance, Barut et al. [34] presented an improved RZT that includes a parabolic distribution for both the in-plane zigzag and transverse displacements in conjunction with an independent assumption of the transverse normal stress. Using Reissner's Mixed Variational Theorem (RMVT), Iurlaro et al. [35] have formulated a similar model by assuming a third-order distribution for the in-plane displacement and a parabolic one for the transverse one. According to Ref. [35], the transverse normal and the transverse shear stresses are assumed a-priori: the former as a cubic function valid across the laminate thickness, the latter obtained by integrating Cauchy's equations. The use of RMVT ensured the transverse shear and normal strain compatibilities, but due to its formulation, some inconsistencies arise when too many kinematic variables are used to interpolate the assumed transverse shear stresses. As an alternative to using the RMVT, the Hellinger-Reissner (HR) theorem has been combined with the RZT kinematics to improve the stress prediction accuracy and avoid numerical inconsistencies. For example, in Groh and Weaver [36,37] work, a higher-order RZT-based formulation was implemented with transverse shear and normal stress assumptions through the HR variational statement, enhancing the stress predictions in highly heterogeneous laminates. More recently, Kutlu et al. [38] have applied the HR variational approach to linear RZT for the stress analysis of laminated composite plates, demonstrating its robustness and applicability to heterogeneous and damaged plates.

It should be noted that the earlier mentioned RZT formulations cannot address more general lamination schemes, such as angle-ply, due to the limitations of the zigzag functions in predicting the transverse shear strain coupling typical of these lay-up configurations. To overcome this limitation, an enhancement in the zigzag functions formulation for RZT has been presented in Ref. [39]. By taking advantage of the intrinsic transverse anisotropy of general lamination schemes, the set of zigzag functions is reformulated and ehanced with two additional coupling functions of the zigzag rotations. The enhanced-RZT (en-RZT) has demonstrated its validity in predicting both static and dynamic structural performances and buckling loads of angle-ply structures [39–41]. Subsequently, the en-RZT has been extended to the analysis of thick general multilayered composite and sandwich plates by Sorrenti and Gherlone [42]. Starting from the displacement field introduced by Iurlaro [35], in the novel en $-$ $\mathrm{RZT}^{(m)}_{\{3,2\}}$ [42], a new set of strain variables is introduced to expresse the assumed transverse shear stress distribution, in order to avoid the limitations of the RMVT. The transverse shear and normal strain compatibilities have been ensured by the Hellinger-Reissner functional, whereas a penalty function is adopted to enforce the compatibility between the new strain variables and those coming from the displacement field. The comparisons for cross-ply and angle-ply laminates with the three-dimensional elasticity solutions provided in Ref. [42] have demonstrated good accuracy of en$-$ $\mathrm{RZT}^{(m)}_{\{3,2\}}$ model in predicting displacements, strain and stress distributions even for the cases where the transverse normal deformability is present.

Although not exhaustive, the provided references report, in most cases, only numerical comparisons with reference results coming from exact elasticity solutions or, when unavailable, high-fidelity three-dimensional FE model solutions. Numerical comparisons with experimental data are rarely found in the open literature. Yan et al. [43] determined the bending and failure characteristics of metallic sandwich beams with corrugated cores through three-point bending tests. In Iurlaro et al. [19,20], a set of moderately thick sandwich beam specimens are subjected to static and dynamic experimental tests whose results are compared with those coming from RZT. For the first time, Ascione and co-workers [44] have experimentally assessed the RZT for the computation of the critical buckling loads of multilayered composite sandwich beams, remarking the greatest accuracy of the RZT than the FSDT. The local and global experimental response of sandwich beams made of GFRP faces and PET foam core has been assessed by Pyrzowski and Sobczyk [45]. Giordano et al. [28] adopted the Digital Image Correlation (DIC) technique to experimentally measure a sandwich beam's full displacement and strain fields under three-point bending test. In Xia et al. [46], the bending performances of sandwich panels with different cores have been assessed experimentally and numerically compared with the results using a FE model. For most of the cited papers, the considered length-to-thickness ratio falls within the range from moderately thick to thin regimes, thus limiting the effect of transverse normal deformability plays a little role. In addition, the numerical comparisons are made with experimentally measured deflections and strains in some discrete points on the external beam surfaces. Moreover, in three-point bending tests for thick sandwich beams, the effect of concentrated load and boundary conditions induce localised peak of strains at the facesheet-core interface that should be monitored to prevent the most common failure mechanisms, e.g. indentation, core shear failure and debonding. For this reason, the emerging use of Distributed Fibre Optic Strain (DFOS) sensors for Structural Health Monitoring (SHM) can be considered an accurate and reliable system to evaluate the strain field at the interfaces in multilayered structures, as testified by Refs. [47–49].

The present paper aims to provide a new experimental assessment for the static analysis response of thick sandwich beams made of aluminium face-sheets and soft foam core. A new mixed beam model for sandwich beams is formulated by taking advantage of the promising mixed-variational procedure adopted in Ref. [42] for plate model. The higher-order displacement field, developed in the en $-$ $\mathrm{RZT}^{(m)}_{\{3,2\}}$ to address thick plate structures, is adapted here for sandwich beams. Subsequently, a novel two-node finite element is formulated using the Hellinger-Reissner variational statement and presented to evaluate the static structural performances of thick sandwich beams. Then, the experimental static campaign on thick sandwich beam specimens with embedded DFOS sensors is reported. Finally, a numerical comparison with the newly developed beam model and high-fidelity, three-dimensional and Timoshenko FE results is presented to highlight the advantages and limitations of the model hypotheses.

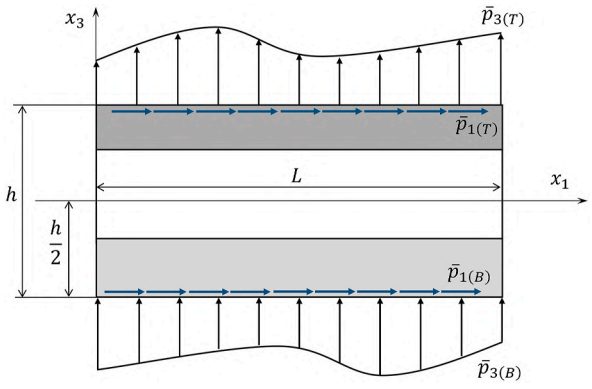

Fig. 1. Beam geometry, reference frame and applied loads.

2. The mixed-{3,2} Refined Zigzag Theory for beams

2.1. Geometrical preliminaries and basics

A multilayered sandwich beam of length L and cross-section area $A = b \times h$ is considered, where b is the width, and h is the thickness. The beam points are referred to a Cartesian orthogonal reference system $\mathbf{X} = (x_1, x_2, x_3)$, where x_1 corresponds to the coordinate of the beam longitudinal axis, with $x_1 \in [0, L]$ and x_3, the transverse coordinate corresponds to the beam thickness, as shown in Fig. 1, where $x_3 \in \left[-h/2,\ +h/2\right] \equiv [x_{3(B)}, x_{3(T)}]$. Let us indicate with the subscript $_{(B)}$ the quantities referred to the bottom surfaces/interfaces, whereas with the subscript $_{(T)}$ those referred to the top ones. The beam is made of N perfectly bonded layers. The thickness and width of each layer and the whole beam are assumed to be constant along the beam axis. The superscript $^{(k)}$ denotes the quantities corresponding to the kth layer (with $k=1, \ldots, N$), whereas the subscript $_{(k)}$ indicates the quantities corresponding to the kth interface, i.e. between the kth and $(k+1)^{th}$ layer. Moreover, let be $h^{(k)} = x_{3(T)}^{(k)} - x_{3(B)}^{(k)} = x_{3(k+1)} - x_{3(k)}$ the thickness of the kth layer.

According to the cylindrical bending assumption, beam deformations are allowed only in the (x_1, x_3) plane, indicating that no out-of-plane displacements are considered. Thus, as reported in Fig. 1, the mechanical loads (unit force/length), denoted with an overbar, applied to the beam's external bottom and top surfaces are the distributed transverse loads, $\bar{p}_{3(B)}(x_1)$ and $\bar{p}_{3(T)}(x_1)$, and the distributed axial loads, $\bar{p}_{1(B)}(x_1)$ and $\bar{p}_{1(T)}(x_1)$.

In the paper, the symbol $(\cdot)_{,i} = \partial(\cdot)/\partial x_i$ stands for the derivative of the function $(\cdot)$ with respect to the x_i coordinate. The superscript $^{\mathrm{T}}$, when associated to vectors and matrices, indicate the transpose operation. Along with the paper, the symbol $\langle(\cdot)\rangle = b\sum_{k=1}^{N}\int_{x_{3(B)}^{(k)}}^{x_{3(T)}^{(k)}}(\cdot)dx_3$ refers to the integral of the quantity $(\cdot)$ over the cross-section area.

Due to the limitations of the classical linear RZT models, which cannot capture the non-linear effects in the through-the-thickness displacement distributions of thick sandwich beams (as observed the three-dimensional solution [3]), a higher-order displacement field based on the RZT kinematics is chosen here to describe the structural response. Consistent with the en $-$ RZT$^{(m)}_{\{3,2\}}$ kinematics (see Ref. [42]), the orthogonal components of the displacement vector for beams read as follows:

$$\begin{aligned} U_1^{(k)}(x_1, x_3) &= u(x_1) + x_3\theta(x_1) + \mu^{(k)}(x_3)\psi(x_1) \\ U_3(x_1, x_3) &= w^{(0)}(x_1) + x_3 w^{(1)}(x_1) + x_3^2 w^{(2)}(x_1) \end{aligned} \tag{1}$$

where, $U_1^{(k)}$ and U_3 are the displacements along x_1 and x_3 directions, respectively. As reported in Ref. [42], the transverse displacement is assumed as a smeared parabolic function of the thickness coordinate independent of the layer. The kinematic variables that appear in Eq. (1) are $u(x_1)$ and $w^{(0)}(x_1)$ (the uniform axial and transverse displacements), $\theta(x_1)$ (the average bending rotation), $\psi(x_1)$ (the zigzag rotation), which are the same quantities of the linear RZT formulation. Moreover, $w^{(1)}(x_1)$ and $w^{(2)}(x_1)$ are new kinematic variables of the transverse displacement for the linear and quadratic term, respectively. Moreover, in Eq. (1), $\mu^{(k)}$ is the third-order piecewise continuous zigzag function whose full expression for beam reads [35,42]:

$$\mu^{(k)}(x_3) = -x_3^2\chi_0 - x_3^3\omega_0 + \varphi^{(k)}(x_3) \tag{2}$$

with

$$\begin{aligned} &\chi_0 = \frac{2\left(\beta^{(1)} + \beta^{(N)} + 2\right)}{3h^2};\ \omega_0 = \frac{1}{2h}\left(\beta^{(N)} - \beta^{(1)}\right); \\ &\varphi^{(k)}(x_3) = \beta^{(k)}(x_3 - x_{3(B)}) + \sum_{q=1}^{k} h^{(q)}\left(\beta^{(q)} - \beta^{(k)}\right)(k = 1, \ldots, N) \end{aligned} \tag{3}$$

$\varphi^{(k)}(x_3)$ is the linear zigzag function and $\beta^{(k)}$ represents the zigzag slope of the kth layer, i.e. $\beta^{(k)} = \varphi_{,3}^{(k)}$, obtained as a result of the partial transverse shear stress continuity at each layer interface (see Ref. [42] for more details on the formulation). It can be noted that the displacement field reported by Eq. (1) for a beam structure derived from the en $-$ RZT$^{(m)}_{\{3,2\}}$ plate model is formally the same as those introduced by Iurlaro et al. [35], except for a different interpretation for the kinematic variables for the transverse displacement.

Consistent with the linear strain-displacement relations, the strain components for the beam structure read:

$$\begin{aligned} \varepsilon_{11}^{(k)}(x_1, x_3) &= u_{,1}(x_1) + x_3\theta_{,1}(x_1) + \mu^{(k)}(x_3)\psi_{,1}(x_1) \\ \varepsilon_{33}(x_1, x_3) &= w^{(1)}(x_1) + 2x_3 w^{(2)}(x_1) \\ \gamma_{13}^{(k)}(x_1, x_3) &= w_{,1}^{(0)}(x_1) + x_3 w_{,1}^{(1)}(x_1) + x_3^2 w_{,1}^{(2)}(x_1) + \theta(x_1) + \mu_{,3}^{(k)}(x_3)\psi(x_1) \end{aligned} \tag{4}$$

Assuming that each layer is made of linear elastic and orthotropic material and assuming the transverse normal stress component to be not negligible, the following beam strain-stress relations (for plane-stress condition) are written in an appropriate mixed form [50]:

$$\begin{Bmatrix} \sigma_{11} \\ \varepsilon_{33} \\ \tau_{13} \end{Bmatrix}^{(k)} = \begin{bmatrix} E_1 & \nu_{13} & 0 \\ -\nu_{13} & \dfrac{1-\nu_{13}\nu_{31}}{E_3} & 0 \\ 0 & 0 & G_{13} \end{bmatrix}^{(k)} \begin{Bmatrix} \varepsilon_{11} \\ \sigma_{33} \\ \gamma_{13} \end{Bmatrix}^{(k)} \tag{5}$$

2.2. Transverse normal and shear stress assumptions

As anticipated, the transverse normal deformability cannot be neglected for thick sandwich structures. In this model, the transverse normal stress is assumed to be a smeared cubic function that satisfies the traction conditions at the bottom and top external beam surfaces. Its expression, which is equivalent to that obtained for the plate model (see Ref. [42]), is here reported for clarity:

$$\sigma_{33}^{a}(x_1, x_3) = \mathbf{P}_{\sigma}(x_3)\mathbf{q}_{\sigma}(x_1) + \mathbf{L}_{\sigma}(x_3)\overline{\mathbf{q}}_{z}(x_1) \tag{6}$$

where

$$\begin{aligned} &\mathbf{L}_{\sigma}(x_3) = \left[\left(\frac{x_3}{h} - \frac{1}{2}\right) \quad \left(\frac{x_3}{h} + \frac{1}{2}\right) \right]; \mathbf{P}_{\sigma}(x_3) = \left[\left(x_3^2 - \frac{h^2}{4}\right) \quad x_3\left(x_3^3 - \frac{h^2}{4}\right) \right]; \\ &\overline{\mathbf{q}}_{z}(x_1)^T = [\,\overline{p}_{3(B)} \quad \overline{p}_{3(T)}\,]; \mathbf{q}_{\sigma}(x_1)^T = [\,\sigma_2^z \quad \sigma_3^z\,] \end{aligned} \tag{7}$$

Additionally, in the present model, transverse shear stress is assumed a-priori to enhance the predictivity capabilities of the transverse shear deformability. Following the methodology adopted in Ref. [42], the assumed transverse shear stress distribution is derived by integrating Cauchy's equations, specialised under the hypothesis of cylindrical bending assumptions while neglecting body forces. For the sake of clarity, the equation reads:

$$\tau_{13}^{a} = -\int_{h} \sigma_{11,1}^{(k)} dx_3 \tag{8}$$

The axial stress that appears in Eq. (8) comes from the constitutive relation given by Eq. (5), with the strains quantities, i.e. the derivatives of the kinematic variables (see Eq. (4)), assumed as new independent variables. According to this assumption, the axial strain is rewritten as follows:

$$\varepsilon_{11}^{(k)}(x_1, x_3) = u_{,1}(x_1) + x_3\theta_{,1}(x_1) + \mu^{(k)}(x_3)\psi_{,1} \rightarrow e(x_1) + x_3 k(x_1) + \mu^{(k)}(x_3)k^{\psi}(x_1) \tag{9}$$

where, $e(x_1)$, $k(x_1)$ and $k^{\psi}(x_1)$ are the introduced new strain variables. Since in Eq. (5) the axial stress is also a function of the assumed transverse normal stress, it cannot be used in Cauchy's equation yet. An intermediate step given by the mixed variational statement is required prior to perform the integration of Eq. (8) to obtain the expression of the assumed transverse shear stress distribution.

2.3. Mixed variational statement: the Hellinger-Reissner functional

In order to obtain the equilibrium equations and a FE formulation of the mixed-beam model $\mathrm{RZT}^{(m)}_{\{3,2\}}$, a mixed-variational principle is necessary due to the inclusion of two independent fields in the $\mathrm{RZT}^{(m)}_{\{3,2\}}$ model: the displacement field (see Eq. (1)) and the transverse stress ones (see Eqs. (6) and (8)). For this purpose, the Hellinger-Reissner (HR) functional [51] can be adopted. According to its definition (see Ref. [51]), the HR functional allows displacements and stresses to vary independently, while still ensuring the strain compatibility conditions between the quantities derived from the displacement and stress fields. This condition, enforced in an integral (or weak) form, improves the accuracy of displacement predictions compared to the Principle of Virtual Displacements (PVDs), and simultaneously provides accurate stress predictions in FE formulation, due to the independent stress field assumption.

By neglecting the work of inertial forces, its expression reads as follows:

$$\delta\Pi = \delta\Pi_{\mathrm{int}} + \delta\Pi_{HR} + \delta\Lambda - \delta\Pi_{ext} = 0 \tag{10}$$

Defining the symbol δ as the virtual variation operator, $\delta\Pi_{\mathrm{int}}$ is the virtual variation of the internal energy. It reads,

$$\delta\Pi_{\mathrm{int}} = \int_{V} \left[\left(\delta\varepsilon_{11}^{(k)}\sigma_{11}^{(k)} + \delta\gamma_{13}^{(k)}\tau_{13}^{a} + \delta\varepsilon_{33}\sigma_{33}^{a} \right) \right] dV \tag{11}$$

Moreover, $\delta\Pi_{HR}$ is the Hellinger-Reissner variational contribution reads:

$$\delta\Pi_{HR} = \int_{V} \left[\delta\tau_{13}^{a}\left(\gamma_{13}^{(k)} - \gamma_{13}^{(k)a}\right) + \delta\sigma_{33}^{a}\left(\varepsilon_{33} - \varepsilon_{33}^{(k)a}\right) \right] dV = \int_{V} \delta\tau_{13}^{a}\left(\gamma_{13}^{(k)} - \gamma_{13}^{(k)a}\right) dV + \delta\Pi_{\sigma_{33}} \tag{12}$$

From a mathematical point of view, in Eq. (12) the assumed stress quantities can be seen as Lagrangian multiplier in the compatibility conditions, ensuring that the strains derived from the displacement field are consistent with the deformation state as

given by the assumed stress field.

In Eqs. (11) and (12) the superscript "a" denotes the assumed stresses and the strains coming from the material constitutive law, i.e. Eq. (5).

The penalty functional in Eq. (10), expressed by the symbol $\delta\Lambda$, enforces in a weak manner the compatibility conditions between the set of new strain variables and the quantities coming from the displacement-strain relations, see Eq. (9). The introduced penalty parameter, i.e. η, plays the role of a weight term in the overall governing functional (in this model $\eta = 10^{-3}$). Its expression, according to the $\mathrm{RZT}^{(m)}_{\{3,2\}}$ model, reads:

$$\delta\Lambda = \frac{1}{\eta}\int_V \left[\left(\delta u_{,1} - \delta e\right)\left(u_{,1} - e\right) + \left(\delta\theta_{,1} - \delta k\right)\left(\theta_{,1} - k\right) + \left(\delta\psi_{,1} - \delta k^{\psi}\right)\left(\psi_{,1} - k^{\psi}\right)\right] dV \tag{13}$$

At last, the virtual work done by the externally applied tractions, $\delta\Pi_{ext}$, reads:

$$\delta\Pi_{ext} = \int_L \bar{p}_{1(T)} U_1^{(N)}(x_{3(T)})dx_1 + \int_L \bar{p}_{1(B)} U_1^{(1)}(x_{3(B)})dx_1 + \int_L \bar{p}_{3(T)} U_3^{(N)}(x_{3(T)})dx_1 + \int_L \bar{p}_{3(B)} U_3^{(1)}(x_{3(B)})dx_1 \tag{14}$$

As previously done for the plate en $-$ $\mathrm{RZT}^{(m)}_{\{3,2\}}$ theory [42], the first step of the beam model formulation is to enforce the transverse normal strain compatibility in the Hellinger-Reissner functional. This condition reads:

$$\delta\Pi_{\sigma_{33}} = \int_V \delta\sigma^a_{33}\left(\varepsilon_{33} - \varepsilon^{(k)a}_{33}\right) dV = 0 \tag{15}$$

Due to the independent assumption of the normal stress field, the condition given by Eq. (15) results in a relationship between the new stress variables and the kinematic ones. Adopting the constitutive material equations, i.e. Eq. (5), the assumed transverse normal strain reads:

$$\varepsilon^a_{33}(x_1, x_3) = S^{(k)}_{33}\sigma^a_{33}(x_1, x_3) - R^{(k)}_{13}\varepsilon^{(k)}_{11}(x_1, x_3) \tag{16}$$

After substituting Eq. (16) into Eq. (15), the transverse normal stress is rewritten as a function of the kinematic variables:

$$\sigma^a_{33}(x_1, x_3) = A^u_\sigma(x_3)u_{,1}(x_1) + A^\theta_\sigma(x_3)\theta_{,1}(x_1) + A^\psi_\sigma(x_3)\psi_{,1}(x_1) + \mathbf{A}^w_\sigma(x_3)\mathbf{w}(x_1) + \mathbf{A}^{q_z}_\sigma(x_3)\overline{\mathbf{q}}_z(x_1) \tag{17}$$

where $\mathbf{w}^T = \begin{bmatrix} w^{(0)} & w^{(1)} & w^{(2)} \end{bmatrix}$. Moreover, the functions of the transverse coordinate that appear in Eq. (17) are reported for the sake of conciseness in Appendix A.

Taking into account the final expression of the transverse normal stress, i.e. Eq. (17) and substituting it into the constitutive relations, i.e. Eq. (5), and adopting the new strain variables, the complete expression of the axial stress reads:

$$\begin{aligned} \sigma^{(k)}_{11} = &\left(E^{(k)}_1 + R_{13}{}^{(k)}A^u_\sigma(x_3)\right)e(x_1) + \left(x_3E^{(k)}_1 + R_{13}{}^{(k)}A^\theta_\sigma(x_3)\right)k(x_1) + \\ &+\left(E^{(k)}_1\mu^{(k)}(x_3) + R_{13}{}^{(k)}A^\psi_\sigma(x_3)\right)k^\psi(x_1) + R_{13}{}^{(k)}\mathbf{A}^w_\sigma(x_3)\mathbf{w}(x_1) + R_{13}{}^{(k)}\mathbf{A}^{q_z}_\sigma(x_3)\overline{\mathbf{q}}_z(x_1) \end{aligned} \tag{18}$$

Substituting Eq. (18) into (8), integrating along the thickness direction and enforcing the equilibrium with the prescribed tractions we obtain:

$$\begin{aligned} &\tau^a_{13}(x_1, x_3) = \bar{p}_{1(B)}(x_1)\left[-1 + \frac{1}{h}\left(x_3 + h/2\right)\right] + \frac{1}{h}\left(x_3 + h/2\right)\bar{p}_{1(T)}(x_1) + \\ &+\widehat{A}^z(x_3)e_{,1}(x_1) + \widehat{B}^z(x_3)k_{,1}(x_1) + \widehat{D}^z(x_3)k^\psi_{,1}(x_1) + \widehat{\mathbf{E}}^z(x_3)\partial\mathbf{w}(x_1) + \widehat{\mathbf{F}}^z(x_3)\partial\overline{\mathbf{q}}_z(x_1) = \\ &\qquad = \mathbf{Z}_p(x_3)\overline{\mathbf{q}}_\mathbf{p}(x_1) + \mathbf{Z}_t(x_3)\mathbf{q}_t(x_1) + \mathbf{Z}_{qz}(x_3)\partial\overline{\mathbf{q}}_z(x_1) \end{aligned} \tag{19}$$

where $\partial\overline{\mathbf{q}}_z(x_1)$ represent the derivatives of the transverse distributed load, i.e. $\partial\overline{\mathbf{q}}_z(x_1)^T = \begin{bmatrix} \bar{p}_{3(B),1} & \bar{p}_{3(T),1} \end{bmatrix}$; $\overline{\mathbf{q}}_\mathbf{p}(x_1)$ is the vector of the prescribed tractions at the bottom and top external surfaces, i.e. $\overline{\mathbf{q}}_\mathbf{p}(x_1)^T = \begin{bmatrix} \bar{p}_{1(B)} & \bar{p}_{1(T)} \end{bmatrix}$; $\mathbf{q}_t(x_1)^T = \begin{bmatrix} e_{,1}(x_1) & k_{,1}(x_1) & k^\psi_{,1}(x_1) & \partial\mathbf{w}(x_1)^T \end{bmatrix}$ is the vector of the derivatives of the strain unknowns and transverse displacement variables. Moreover, $\partial\mathbf{w}(x_1)^T = \begin{bmatrix} w^{(0)}_{,1} & w^{(1)}_{,1} & w^{(2)}_{,1} \end{bmatrix}$.

By substituting the expression of the displacement field, i.e. Eq. (1), into the strain-displacements relations and taking into account the mixed material constitutive equations, i.e. Eq. (5), the assumed transverse normal, i.e. Eq. (17), and transverse shear, i.e. Eq. (19), stresses into the variational statement Eq. (10) and integrating by parts, the governing equations of the $\mathrm{RZT}^{(m)}_{\{3,2\}}$ model are obtained:

$$
\begin{aligned}
&\delta u : N_{,1} + {}^{1}/_{\eta}\left(u_{,11} - e_{,1}\right) + \overline{p}_1 = 0\\
&\delta w^{(0)} : Q^{w0}_{,1} - N^{z}_{1} - \widehat{Q}^{w0} - \left(\widehat{D}^{p}_{11}\overline{p}_{1(B),1} + \widehat{D}^{p}_{13}\overline{p}_{1(T),1}\right) - \left(\widehat{D}^{q}_{11}\overline{p}_{3(B),11} + \widehat{D}^{q}_{12}\overline{p}_{3(T),11}\right) + \overline{q}_3 = 0\\
&\delta w^{(1)} : Q^{w1}_{,1} - N^{z}_{2} - \widehat{Q}^{w1} - \left(\widehat{D}^{p}_{21}\overline{p}_{1(B),1} + \widehat{D}^{p}_{23}\overline{p}_{1(T),1}\right) - \left(\widehat{D}^{q}_{11}\overline{p}_{3(B),11} + \widehat{D}^{q}_{12}\overline{p}_{3(T),11}\right) + \frac{h}{2}\left(\overline{p}_{3(T)} - \overline{p}_{3(B)}\right) = 0\\
&\delta w^{(2)} : Q^{w2}_{,1} - N^{z}_{3} - \widehat{Q}^{w2} - \left(\widehat{D}^{p}_{31}\overline{p}_{1(B),1} + \widehat{D}^{p}_{33}\overline{p}_{1(T),1}\right) - \left(\widehat{D}^{q}_{31}\overline{p}_{3(B),11} + \widehat{D}^{q}_{32}\overline{p}_{3(T),11}\right) + \frac{h^2}{4}\overline{q}_3 = 0\\
&\delta\theta : M_{,1} - Q + {}^{1}/_{\eta}\left(\theta_{,11} - k_{,1}\right) + \overline{m}_1 = 0\\
&\delta\psi : M^{\phi}_{,1} - Q^{\phi} + \frac{1}{\eta}\left(\psi_{,11} - k^{\psi}_{,1}\right) = 0\\
&\delta e : -{}^{1}/_{\eta}\left(e - u_{,1}\right) - \left(\widehat{A}^{p}_{11}\overline{p}_{1(B),1} + \widehat{A}^{p}_{13}\overline{p}_{1(T),1}\right) - \left(\widehat{A}^{q}_{11}\overline{p}_{3(B),11} + \widehat{A}^{q}_{12}\overline{p}_{3(T),11}\right) + E^{HR} = 0\\
&\delta k : -{}^{1}/_{\eta}\left(k - \theta_{,1}\right) - \left(\widehat{B}^{p}_{11}\overline{p}_{1(B),1} + \widehat{B}^{p}_{13}\overline{p}_{1(T),1}\right) - \left(\widehat{B}^{q}_{11}\overline{p}_{3(B),11} + \widehat{B}^{q}_{12}\overline{p}_{3(T),11}\right) + K^{HR} = 0\\
&\delta k^{\psi} : -{}^{1}/_{\eta}\left(k^{\psi} - \psi_{,1}\right) - \left(\widehat{C}^{p}_{11}\overline{p}_{1(B),1} + \widehat{C}^{p}_{13}\overline{p}_{1(T),1}\right) - \left(\widehat{C}^{q}_{11}\overline{p}_{3(B),11} + \widehat{C}^{q}_{12}\overline{p}_{3(T),11}\right) + K^{HR}_{\psi} = 0
\end{aligned}
\tag{20}
$$

along with the consistent boundary conditions:

$$
\begin{aligned}
&u = \overline{u} \quad \text{on } x_1 = 0, L \quad \vee \overline{N} + {}^{1}/_{\eta}\left(u_{,1} - e\right) \quad \text{on } x_1 = 0, L\\
&w^{(0)} = \overline{w}^{(0)} \quad \text{on } x_1 = 0, L \quad \vee \overline{Q}^{w0} + \overline{Q}^{w0}_{1} HR \quad \text{on } x_1 = 0, L\\
&w^{(1)} = \overline{w}^{(1)} \quad \text{on } x_1 = 0, L \quad \vee \overline{Q}^{w1} + \overline{Q}^{w1}_{1} HR \quad \text{on } x_1 = 0, L\\
&w^{(2)} = \overline{w}^{(2)} \quad \text{on } x_1 = 0, L \quad \vee \overline{Q}^{w2} + \overline{Q}^{w2}_{1} HR \quad \text{on } x_1 = 0, L\\
&\theta = \overline{\theta} \quad \text{on } x_1 = 0, L \quad \vee \overline{M} + {}^{1}/_{\eta}\left(\theta_{,1} - k_{11}\right) \quad \text{on } x_1 = 0, L\\
&\psi = \overline{\psi} \quad \text{on } x_1 = 0, L \quad \vee \overline{M}^{\phi} + {}^{1}/_{\eta}\left(\psi_{,1} - k^{\psi}\right) \quad \text{on } x_1 = 0, L\\
&e = \overline{e} \quad \text{on } x_1 = 0, L \quad \vee \overline{E}^{e}_{1} HR \quad \text{on } x_1 = 0, L\\
&k = \overline{k} \quad \text{on } x_1 = 0, L \quad \vee \overline{K}^{k}_{1} HR \quad \text{on } x_1 = 0, L\\
&k^{\psi} = \overline{k}^{\psi} \quad \text{on } x_1 = 0, L \quad \vee \overline{K}^{k\psi}_{1} HR \quad \text{on } x_1 = 0, L
\end{aligned}
\tag{21}
$$

where the resultant forces and moments are defined as:

$$
\begin{aligned}
&\left(N, M, M^{\phi}\right) = \langle\left(1, x_3, \mu^{(k)}(x_3)\right)\sigma^{(k)}_{11}\rangle;\\
&\mathbf{N}^{z} = \langle \mathbf{H}^{z\,T}_{,3}\sigma^{a}_{33}\rangle;\\
&\left(\mathbf{Q}^{w}, Q, Q^{\phi}\right) = \langle\left(\mathbf{H}^{zT}, 1, \mu^{(k)}_{,3}\right)\tau^{a}_{13}\rangle
\end{aligned}
\tag{22}
$$

Moreover, in Eq. (20) the sum of the distributed loads and moments appear that are defined as follows:

$$
\begin{aligned}
&\overline{p}_1 = \overline{p}_{1(B)} + \overline{p}_{1(T)};\\
&\overline{m}_1 = h/2\left(\overline{p}_{1(T)} - \overline{p}_{1(B)}\right);\\
&\overline{q}_3 = \overline{p}_{3(B)} + \overline{p}_{3(T)}
\end{aligned}
\tag{23}
$$

By using the mixed material constitutive relations, i.e. Eq. (5), the assumed transverse normal and shear stresses, i.e. Eqs. (17) and (19), the $\mathrm{RZT}^{(m)}_{\{3,2\}}$ beam constitutive relations in terms of the kinematic and strains unknowns are expressed as follows:

$$
\begin{aligned}
&N = \widetilde{A}u_{,1} + \widetilde{B}\theta_{,1} + \widetilde{A}^{\phi}\psi_{,1} + \widetilde{\mathbf{A}}^{w}\mathbf{w} + \widetilde{\mathbf{A}}^{qz}\overline{\mathbf{q}}_z\\
&M = \widetilde{C}u_{,1} + \widetilde{D}\theta_{,1} + \widetilde{B}^{\phi}\psi_{,1} + \widetilde{\mathbf{B}}^{w}\mathbf{w} + \widetilde{\mathbf{B}}^{qz}\overline{\mathbf{q}}_z\\
&M^{\phi} = \widetilde{E}^{\phi}u_{,1} + \widetilde{F}^{\phi}\theta_{,1} + \widetilde{G}^{\phi}\psi_{,1} + \widetilde{\mathbf{C}}^{w}\mathbf{w} + \widetilde{\mathbf{C}}^{qz}\overline{\mathbf{q}}_z
\end{aligned}
\tag{24}
$$

$$
\mathbf{N}^{z} = \mathbf{A}^{Nz}u_{,1} + \mathbf{B}^{Nz}\theta_{,1} + \mathbf{C}^{Nz}\psi_{,1} + \mathbf{D}^{Nz}\mathbf{w} + \mathbf{E}^{Nz}\overline{\mathbf{q}}_z \tag{25}
$$

$$\begin{aligned} \mathbf{Q}^{w} &= \widehat{\mathbf{A}}^{wT} e_{,1} + \widehat{\mathbf{B}}^{wT} k_{,1} + \widehat{\mathbf{C}}^{wT} k_{,1}^{\psi} + \widehat{\mathbf{D}}^{wT} \partial \mathbf{w} + \widehat{\mathbf{E}}^{w} \partial \overline{\mathbf{q}}_{z} + \widehat{\mathbf{P}}^{w} \overline{\mathbf{q}}_{\mathbf{p}} \\ Q &= \widehat{A}^{\theta} e_{,1} + \widehat{B}^{\theta} k_{,1} + \widehat{C}^{\theta} k_{,1}^{\psi} + \widehat{\mathbf{D}}^{\theta T} \partial \mathbf{w} + \widehat{\mathbf{E}}^{\theta} \partial \overline{\mathbf{q}}_{z} + \widehat{\mathbf{P}}^{\theta} \overline{\mathbf{q}}_{\mathbf{p}} \\ Q^{\phi} &= \widehat{A}^{\psi} e_{,1} + \widehat{B}^{\psi} k_{,1} + \widehat{C}^{\psi} k_{,1}^{\psi} + \widehat{\mathbf{D}}^{\psi T} \partial \mathbf{w} + \widehat{\mathbf{E}}^{\psi} \partial \overline{\mathbf{q}}_{z} + \widehat{\mathbf{P}}^{\psi} \overline{\mathbf{q}}_{\mathbf{p}} \end{aligned} \tag{26}$$

For sake of clarity, the other quantities that appear in the governing equations, boundary conditions and constitutive relations are reported in Appendix C.

3. Finite element formulation

This Section presents the formulation of a simple two-node beam element based on the $\mathrm{RZT}^{(m)}_{\{3,2\}}$.

The kinematic and strain variables that appear in the mixed variational statement (see Eqs. (11)–(13)) do not exceed the first spatial derivative. Thus, efficient C^0 – continuous shape functions can be adopted in the finite formulation. Since this work focuses on the study of thick to very thick multilayered sandwich beams, the influence of shear-locking is not considered, and the well-known strategies commonly adopted to mitigate its effect on slender beams are not addressed here. From a mathematical point of view, the mixed-finite element formulation introduces a typical saddle-point problem governed by complex methematical relations, as detailed by Babuska [52] and Brezzi [53]. This issue, also known as the Babuska-Brezzi condition, requires an appropriate selection of the possible shape functions in the element formulation in order to avoid stability issues and inconsistencies on the final numerical results. Thus, from a practical point of view, a condition necessary and sufficient to the problem solvability is that the number of the kimeatic degrees of freedom (dof) must be equal or larger than the dofs' number used for the stress approximations.

3.1. Interpolation scheme

In virtue of the previous considerations regarding the variational statement and the Babuska-Brezzi condition, the simplest and lowest order beam element is the isoparametric one, which is formulated by approximating each unknown variable using the linear Lagrangian polynomials. By grouping the kinematic and the strain unknown variables into two different vectors, i.e. $\mathbf{d}_d{}^T = \begin{bmatrix} u & w^{(0)} & w^{(1)} & w^{(2)} & \theta & \psi \end{bmatrix}$ and $\mathbf{d}_s{}^T = \begin{bmatrix} e & k & k^{\psi} \end{bmatrix}$, we can write:

$$\begin{Bmatrix} \mathbf{d}_d(x_1) \\ \mathbf{d}_s(x_1) \end{Bmatrix} = \begin{bmatrix} \mathbf{N}_d(x_1) & \mathbf{0} \\ \mathbf{0} & \mathbf{N}_s(x_1) \end{bmatrix} \begin{Bmatrix} \mathbf{q}_d^{(e)} \\ \mathbf{q}_s^{(e)} \end{Bmatrix} \tag{27}$$

where the shape function matrices, e.g. $\mathbf{N}_d(x_1)$ and $\mathbf{N}_s(x_1)$ that appears in Eq. (27), read as follows

$$\mathbf{N}_d = \begin{bmatrix} \mathbf{L} & \mathbf{0} & \mathbf{0} & \mathbf{0} \\ & \mathbf{L}^{w} & \mathbf{0} & \mathbf{0} \\ & & \mathbf{L} & \mathbf{0} \\ sym. & & & \mathbf{L} \end{bmatrix}; \quad \mathbf{N}_s = \begin{bmatrix} \mathbf{L} & \mathbf{0} & \mathbf{0} \\ & \mathbf{L} & \mathbf{0} \\ sym. & & \mathbf{L} \end{bmatrix}; \quad \mathbf{L}^{w} = \begin{bmatrix} \mathbf{L} & \mathbf{0} & \mathbf{0} \\ & \mathbf{L} & \mathbf{0} \\ sym. & & \mathbf{L} \end{bmatrix} \tag{28}$$

Moreover, in Eq. (27), the vectors of the elemental nodal degree of freedoms reads:

$$\mathbf{q}_d^{(e)T} = \begin{bmatrix} \mathbf{q}^{uT} & \mathbf{q}^{wT} & \mathbf{q}^{\theta T} & \mathbf{q}^{\psi T} \end{bmatrix}; \quad \mathbf{q}_s^{(e)T} = \begin{bmatrix} \mathbf{q}^{eT} & \mathbf{q}^{kT} & \mathbf{q}^{k\psi T} \end{bmatrix} \tag{29}$$

and, for each sub-vector, we can write:

$$\mathbf{q}^{uT} = \begin{bmatrix} u_1 & u_2 \end{bmatrix}; \ \mathbf{q}^{wT} = \begin{bmatrix} w_1^{(0)} & w_2^{(0)} & w_1^{(1)} & w_2^{(1)} & w_1^{(2)} & w_2^{(2)} \end{bmatrix}; \ \mathbf{q}^{\theta T} = \begin{bmatrix} \theta_1 & \theta_2 \end{bmatrix}; \ \mathbf{q}^{\psi T} = \begin{bmatrix} \psi_1 & \psi_2 \end{bmatrix} \tag{30}$$

$$\mathbf{q}^{eT} = \begin{bmatrix} e_1 & e_2 \end{bmatrix}; \ \mathbf{q}^{kT} = \begin{bmatrix} k_1 & k_2 \end{bmatrix}; \ \mathbf{q}^{k\psi T} = \begin{bmatrix} k_1^{\psi} & k_2^{\psi} \end{bmatrix} \tag{31}$$

As anticipated, in Eq (28) the elemental shape functions matrices are constituted by the Lagrangian shape functions defined in the natural coordinate system, i.e. $\xi = 2x_1/L^{(e)} - 1 \in [-1,1]$, where $L^{(e)}$ represents the beam element length. The vector of the linear shape functions is defined as follows,

$$\mathbf{L}(\xi) = \begin{bmatrix} L_1(\xi) & L_2(\xi) \end{bmatrix} = \begin{bmatrix} \frac{1}{2}(1-\xi) & \frac{1}{2}(1+\xi) \end{bmatrix} \tag{32}$$

3.2. Elemental stiffness and force vector

The elemental stiffness matrix and load vector of the 2-noded mixed-{3,2}-RZT beam element, here named with 2B − $\mathrm{RZT}^{(m)}_{\{3,2\}}$, are obtained by adopting the finite element approximation, i.e. Eq. (27), into the mixed variational statement given by Eq. (10). According to this procedure, the linear strain-displacement relations, Eq. (4), for an eth element read as follows:

$$\varepsilon_{11}^{(k)(e)} = \left[\begin{array}{ccc} \mathbf{L}_{,1} & x_3\mathbf{L}_{,1} & \mu^{(k)}\mathbf{L}_{,1} \end{array}\right] \left\{\begin{array}{c} \mathbf{q}^u \\ \mathbf{q}^\theta \\ \mathbf{q}^\psi \end{array}\right\}^{(e)} ; \gamma_{13}^{(e)} = \left[\begin{array}{ccc} \mathbf{H}^z\mathbf{L}_{,1}^w & \mathbf{L} & \partial_3\mu^{(k)}\mathbf{L} \end{array}\right] \left\{\begin{array}{c} \mathbf{q}^w \\ \mathbf{q}^\theta \\ \mathbf{q}^\psi \end{array}\right\}^{(e)} ; \varepsilon_{33}^{(e)} = \mathbf{H}_{,3}^z\mathbf{L}^w\mathbf{q}^{w(e)} \tag{33}$$

whereas the elemental assumed transverse normal and shear stresses, i.e. Eqs. (17) and (19), follow

$$\sigma_{33}^{a\ (e)} = \left\lfloor A_\sigma^u\mathbf{L}_{,1} \quad \mathbf{A}_\sigma^w\mathbf{L}^w \quad A_\sigma^\theta\mathbf{L}_{,1} \quad A_\sigma^\psi\mathbf{L}_{,1} \right\rfloor \mathbf{q}_d^{(e)} + \mathbf{A}_\sigma^{q_z}\overline{\mathbf{q}}_z \tag{34}$$

$$\tau_{13}^{a\ (e)} = \left[\begin{array}{cccc} \widehat{\mathbf{E}}^z\mathbf{L}_{,1}^w & \widehat{A}^z\mathbf{L}_{,1} & \widehat{B}^z\mathbf{L}_{,1} & \widehat{D}^z\mathbf{L}_{,1} \end{array}\right] \left\{\begin{array}{c} \mathbf{q}^w \\ \mathbf{q}_s \end{array}\right\}^{(e)} + \widehat{\mathbf{F}}^z\partial\overline{\mathbf{q}}_z + \mathbf{Z}_p\overline{\mathbf{p}} \tag{35}$$

The elemental assumed transverse shear strain in the Hellinger-Reissner term of the variational statement (see Eq. (12)) can be related to Eq. (35) with the material constitutive relation Eq. (5). Similarly, the elemental axial stress is obtained by substituting the elemental axial strain of Eq. (33) and the transverse normal stress, i.e. Eq. (34), into Eq. (5).

By proceeding with the appropriate substitutions and adopting the notation introduced by Eq. (27) to highlight the terms of the two groups of unknown variables, the discretised equilibrium equations are expressed as follows:

$$\mathbf{K}^{(e)}\mathbf{q}^{(e)} = \left[\begin{array}{cc} \mathbf{K}_{dd}^{(e)} & \mathbf{K}_{ds}^{(e)} \\ \mathbf{K}_{ds}^{(e)\,T} & \mathbf{K}_{ss}^{(e)} \end{array}\right] \left\{\begin{array}{c} \mathbf{q}_d^{(e)} \\ \mathbf{q}_s^{(e)} \end{array}\right\} = \left\{\begin{array}{c} \mathbf{F}_d^{(e)} \\ \mathbf{F}_s^{(e)} \end{array}\right\} = \mathbf{F}^{(e)} \tag{36}$$

where the full expressions of the matrices and vectors in Eq. (36) are reported for clarity in Appendix D. Since no strategies to mitigate the shear locking problem are implemented, given that the numerical model is designed to study thick structures, full integration of stiffness matrix and load vector requires a two-point Gauss quadrature.

Note that if a concentrated force of intensity $\overline{F}$ (defined as positive if it agrees with x_3 axis direction) is applied on the outer top/bottom external beam surfaces in the correspondence of a generic nth node, the nodal load vector, expressed with the vector $\mathbf{F}_{conc}$, for that specific nth node reads:

$$\mathbf{F}_{conc}^T = \left\lfloor 0 \quad \frac{\overline{F}}{2} \pm\frac{h}{2}\frac{\overline{F}}{2}\frac{h^2}{4}\frac{\overline{F}}{2}0000 \right\rfloor \tag{37}$$

where the sign $\pm$ in Eq. (37) indicates if the force is applied on the top (+) or on the bottom (−) beam surfaces.

According to this formulation, this element involve eighteen dofs (nine dofs for each node), which could be computationally expensive. Therefore, it is possible to adopt the static condensation technique to reduce the computational cost but maintaing the same numerical accuracy.

The second line of Eq. (36) could be solved statically by making $\mathbf{q}_s^{(e)}$ depending on the $\mathbf{q}_d^{(e)}$ variables. It reads:

$$\mathbf{K}_{ds}^{(e)\,T}\mathbf{q}_d^{(e)} + \mathbf{K}_{ss}^{(e)}\mathbf{q}_s^{(e)} = \mathbf{F}_s^{(e)} \rightarrow \mathbf{q}_s^{(e)} = \mathbf{K}_{ss}^{(e)^{-1}}\mathbf{F}_s^{(e)} - \mathbf{K}_{ss}^{(e)^{-1}}\mathbf{K}_{ds}^{(e)\,T}\mathbf{q}_d^{(e)} \tag{38}$$

Substituting Eq. (38) into Eq. (36), it yields a new expression of the equations of motions:

$$\left(\mathbf{K}_{dd}^{(e)} - \mathbf{K}_{ds}^{(e)}\mathbf{K}_{ss}^{(e)^{-1}}\mathbf{K}_{ds}^{(e)\,T}\right)\mathbf{q}_d^{(e)} = \mathbf{F}_d^{(e)} - \mathbf{K}_{ds}^{(e)}\mathbf{K}_{ss}^{(e)^{-1}}\mathbf{F}_s^{(e)} \tag{39}$$

Moreover,

$$\widehat{\mathbf{K}}_{dd}^{(e)}\mathbf{q}_d^{(e)} = \widehat{\mathbf{F}}_d^{(e)} \tag{40}$$

with $\widehat{\mathbf{K}}_{dd}^{(e)} = \left(\mathbf{K}_{dd}^{(e)} - \mathbf{K}_{ds}^{(e)}\mathbf{K}_{ss}^{(e)^{-1}}\mathbf{K}_{ds}^{(e)\,T}\right)$ and $\widehat{\mathbf{F}}_d^{(e)} = \mathbf{F}_d^{(e)} - \mathbf{K}_{ds}^{(e)}\mathbf{K}_{ss}^{(e)^{-1}}\mathbf{F}_s^{(e)}$.

This procedure reduces the overall number of elemental dofs from eighteen to twelve. Thus, the final topology of 2B− $\mathrm{RZT}_{\{3,2\}}^{(m)}$ element is resumed in Fig. 2.

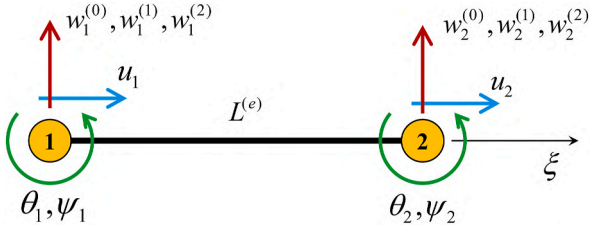

Fig. 2. Topology of the 2B − $\mathrm{RZT}_{\{3,2\}}^{(m)}$ element.

For clarity, the procedure to formulate the 2B – $\mathrm{RZT}^{(m)}_{\{3,2\}}$ element is summarized in the flowchart shown in Fig. 3.

4. Numerical assessment

In this section, the numerical and experimental results are presented and compared.

Firstly, a static analysis was performed to assess the predictivity capabilities of the 2B – $\mathrm{RZT}^{(m)}_{\{3,2\}}$ finite elements, comparing them with the results coming from the analytical $\mathrm{RZT}^{(m)}_{\{3,2\}}$ solution and the three-dimensional exact one given by Pagano [3]. Subsequently, the results coming from the experimental campaign are compared with those obtained by the 2B – $\mathrm{RZT}^{(m)}_{\{3,2\}}$ elements and high-fidelity FE NASTRAN models.

4.1. Convergence analysis and numerical comparison

A multilayered symmetric cross-ply sandwich beam (B0) is considered in this numerical assessment. By considering b=1 mm, Tables 1 and 2 report the materials and the laminate stacking sequence.

The sandwich beam is simply supported on both edges and, according to the $\mathrm{RZT}^{(m)}_{\{3,2\}}$ model, the boundary conditions are specified as follows:

$$\begin{aligned} &@x_1 = 0, L \\ &w^{(0)} = w^{(1)} = w^{(2)} = e = k = k^{\psi} = 0 \\ &N + {}^{1}/_{\eta}\left(u_{,1} - e\right) = M + {}^{1}/_{\eta}\left(\theta_{,1} - k\right) = M^{\phi} + {}^{1}/_{\eta}\left(\psi_{,1} - k^{\psi}\right) = 0 \end{aligned} \tag{41}$$

The numerical results provided for this model assume a transverse distributed load applied to the bottom and top beam surfaces having the following expressions:

$$\begin{aligned} &\overline{p}_{3(B)}(x_1) = \overline{q}_{3(B)} \sin(\pi/L x_1) \\ &\overline{p}_{3(T)}(x_1) = \overline{q}_{3(T)} \sin(\pi/L x_1) \end{aligned} \tag{42}$$

where $\overline{q}_{3(B)}$ and $\overline{q}_{3(T)}$ are the maximum values. In this configuration, the axial bottom and top tractions are null, i.e. $\overline{p}_{1(B)} = \overline{p}_{1(T)} = 0$, and the transverse load is applied only on the top beam surface, i.e. $\overline{q}_{3(B)} = 0$ and $\overline{q}_{3(T)} = -10$ MPa.

For this load configuration, the exact analytical solution using the Navier's method able to satisfy both governing equations and boundary conditions of $\mathrm{RZT}^{(m)}_{\{3,2\}}$ model involves the following trigonometric expansions:

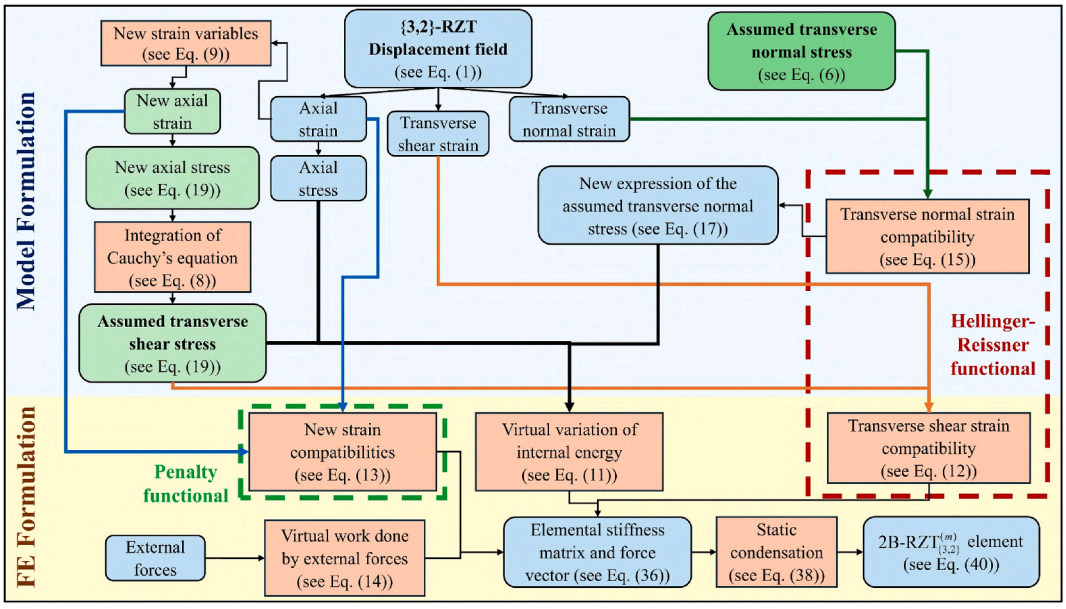

Fig. 3. Flowchart of the 2B – $\mathrm{RZT}^{(m)}_{\{3,2\}}$ element formulation.

Table 1
Material nomenclature and properties. The elastic moduli are in MPa.

Material Name	E_1	E_2	E_3	ν_{12}	ν_{13}	ν_{23}	G_{12}	G_{13}	G_{23}
A	110000	7857	7857	0.33	0.33	0.49	3292	3292	1292
B	40.3	40.3	40.3	0.3	0.3	0.3	12	12	12

Table 2
Laminate stacking sequences and nomenclature. The orientations are in degree.

Laminate ID	Normalised thickness $\boldsymbol{h}^{(k)}/\boldsymbol{h}$	Lamina materials	Lamina orientations [°]
B0	0.05/0.05/0.8/0.05/0.05	A/A/B/A/A	0/90/Core/90/0

$$
\begin{aligned}
&u_1(x_1) = U\cos(\lambda x_1);\\
&w^{(0)}(x_1) = W^{(0)}\sin(\lambda x_1);\\
&w^{(1)}(x_1) = W^{(1)}\sin(\lambda x_1);\\
&w^{(2)}(x_1) = W^{(2)}\sin(\lambda x_1);\\
&\theta(x_1) = \Theta\cos(\lambda x_1);\\
&\psi(x_1) = \Psi\cos(\lambda x_1);\\
&e(x_1) = E\sin(\lambda x_1);\\
&k(x_1) = K\sin(\lambda x_1);\\
&k^{\psi}(x_1) = K^{\psi}\sin(\lambda x_1);
\end{aligned}
\tag{43}
$$

where $\lambda = \pi/L$.

If not otherwise specified, the numerical results are expressed in non-dimensional quantities as follows:

$$
\begin{aligned}
&\overline{U}_1 = 1000\frac{E_2^{(1)}h^2}{\overline{p}_3 L^3}U_1; \quad \overline{U}_3 = 100\frac{E_2^{(1)}h^3}{\overline{p}_3 L^4}U_3;\\
&\{\overline{\sigma}_{11},\overline{\sigma}_{33}\} = \frac{h^2\{\sigma_{11},\sigma_{33}\}}{\overline{p}_3 L^2}; \quad \overline{\tau}_{13} = 10\frac{h\tau_{13}}{\overline{p}_3 L};
\end{aligned}
\tag{44}
$$

where $\overline{p}_3 = \overline{q}_{3(B)} + \overline{q}_{3(T)}$.

In this first numerical example, the convergence behaviour of the $2B-\mathrm{RZT}^{(m)}_{\{3,2\}}$ elements for beam B0 is examined for the length-to-thickness ratios (L/h): 4, 20 and 100. For reference, the analytical results of the non-dimensional maximum transverse displacements evaluated at the mid-length of the beam on the top surface using the new $\mathrm{RZT}^{(m)}_{\{3,2\}}$ model and the classical RZT [54], are reported in Table 3. It is worth noting in Table 3 that for thin sandwich beams with a length-to-thickness ratio higher than 20, the difference in the maximum transverse deflection between the $\mathrm{RZT}^{(m)}_{\{3,2\}}$ new model and the RZT is minimal. In fact, in these cases, the effect of the transverse normal deformability is negligible, and the $\mathrm{RZT}^{(m)}_{\{3,2\}}$ new model correctly converge to the RZT solution, as expected.

Indicating with N_e the number of elements along the beam axis, different discretizations are considered in this FE convergence study: 16, 32, 64, 128, 256, 512, 1024, 2048 and 4096. Fig. 4 reports the convergence rates, expressed as ratio between the FE value and the analytical one using the $\mathrm{RZT}^{(m)}_{\{3,2\}}$ model (analytical reference values are given in Table 3).

Except for coarse FE discretizations, i.e. those with fewer than 16 element, Fig. 4 shows that the $2B-\mathrm{RZT}^{(m)}_{\{3,2\}}$ elements rapidly converge to the analytical solution for all the length-to-thickness ratios investigated. It is also worth noting that the $2B-\mathrm{RZT}^{(m)}_{\{3,2\}}$ elements perform well in thin regimes, where the shear locking may cause numerical problems.

Taking advantage of the convergence analysis and paying particular attention on thick regime, in this second example, a thick ($L/h = 4$) sandwich beam with B0 lay-up is discretised using 1000 $2B-\mathrm{RZT}^{(m)}_{\{3,2\}}$ elements. The through-the-thickness distributions of the stress quantities are evaluated at the centroid of each element and considering that the mesh is highly refined, the accuracy of this choice can be deduced acceptable. Moreover, the through-the-thickness distribution of axial and transverse displacements are

Table 3
Analytical values for non-dimensional maximum transverse displacements ($\overline{U}_3^{An.}$) for simply supported beam B0 under transverse sinusoidal load.

	L/h		
Model	4	20	100
$\mathrm{RZT}^{(m)}_{\{3,2\}}$	334.461	17.866	3.664
RZT [54]	313.204	17.809	3.640

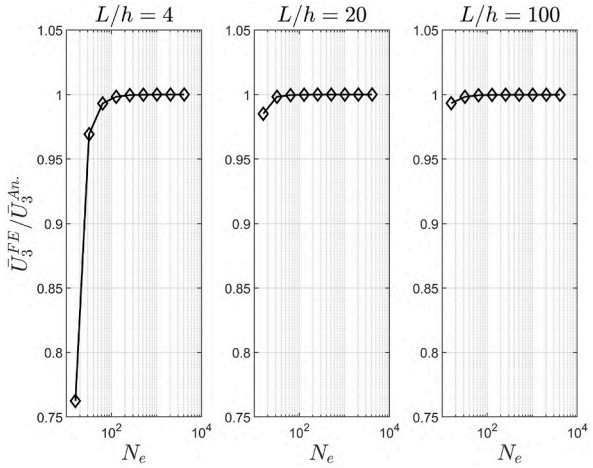

Fig. 4. Convergence rates of $2B-RZT^{(m)}_{\{3,2\}}$ elements for B0 beam, with length-to-thickness ratios of 4, 20 and 100.

evaluated in points corresponding to a mesh discretization node.

The performances of the $2B-RZT^{(m)}_{\{3,2\}}$ in predicting the distributions of displacements and stresses for a multilayered sandwich beam are reported in Fig. 5. Additionally, for refence purposes, Fig. 5 presents the results obtained using the analytical solution of the classical RZT formulation [54], in which the higher-order effects and the transverse normal deformations are neglected. In fact, no results for the through-the-thickness distribution for the transverse normal stress, i.e. σ_{33}, are reported in Fig. 5e. The through-the-thickness distributions of axial displacement and axial stress obtained with $RZT^{(m)}_{\{3,2\}}$ and FE $2B-RZT^{(m)}_{\{3,2\}}$ models are very close with those obtained using classical RZT. However, the results obtained from analytical $RZT^{(m)}_{\{3,2\}}$ and FE $2B-RZT^{(m)}_{\{3,2\}}$ models are remarkably closer to those obtained using the reference three-dimensional exact solution provided by Pagano [3]. Moreover, the classical RZT cannot predict the parabolic thickness-wise distribution of the transverse displacement, that is well predicted by both $RZT^{(m)}_{\{3,2\}}$ model and $2B-RZT^{(m)}_{\{3,2\}}$ elements. Thanks to its mixed formulation using the Hellinger-Reissner functional, the $RZT^{(m)}_{\{3,2\}}$ and $2B-RZT^{(m)}_{\{3,2\}}$ elements demonstrate superior predictive capabilities of the transverse shear stress distribution without using the *a-posteriori* stress recovery procedure, as done in the classical RZT. These advantageous aspects and good convergence behaviour make the novel $RZT^{(m)}_{\{3,2\}}$ formulation and $2B-RZT^{(m)}_{\{3,2\}}$ suitable for experimental comparisons.

5. Experimental assessment

This Section describes the experimental assessment of the developed beam finite element with three- and four-point bending tests performed on thick beam specimens. The experimental activity has been conducted at the LAQ-AERMEC laboratory of the Mechanical and Aerospace Engineering Department (DIMEAS) of the Politecnico di Torino. The sandwich beam specimens have been manufactured by the Department of Science and Aerospace Technology of Politecnico di Milano.

5.1. Beam specimens and material mechanical properties

The beam specimens present a multilayered sandwich scheme, typically adopted for aeronautical applications. Two face-sheets of EN AW7075 (T6) Aluminium alloy (Ergal) have been separated by a thick IG-31 Rohacell® polymethacrylamide foam core. Each beam specimen has a 3 mm face-sheet thickness bonded to the core layer with a 0.25 mm 3M® Scotch-Weld® Structural Adhesive Film AF 163-2K.

In order to investigate the effect of the length-to-thickness ratio in bending analysis, different lengths have been considered. Let us denote with h_f the thickness of each face-sheet, with h_c the thickness of the core layer, obtained as the difference between the total thickness h and the Ergal face-sheet thicknesses. Moreover, let us denote the beam length between the supported cylinders with the symbol L_{eff}. In this study, it has been chosen to leave 20 mm of beam length to each edge, i.e. $L_{eff} = L - 40$ mm. Table 4 reports the nomenclature and beam dimensions (average values of ten measures in different positions along the beam length).

In order to perform a proper comparison between the numerical models and the experimental results, a material characterisation of the Ergal Aluminum alloy and Rohacell® foam has been conducted. For this purpose, a second group of beam specimens has been manufactured to evaluate their mechanical properties experimentally through bending tests. Except for the adhesive layer, whose properties have been taken from the producer datasheet (see, Ref. [55]), the details of the characterisation methodology can be found in Ref. [56].

For the sake of brevity, the results of the experimental characterisation are reported in Table 5. In addition, these values are used in

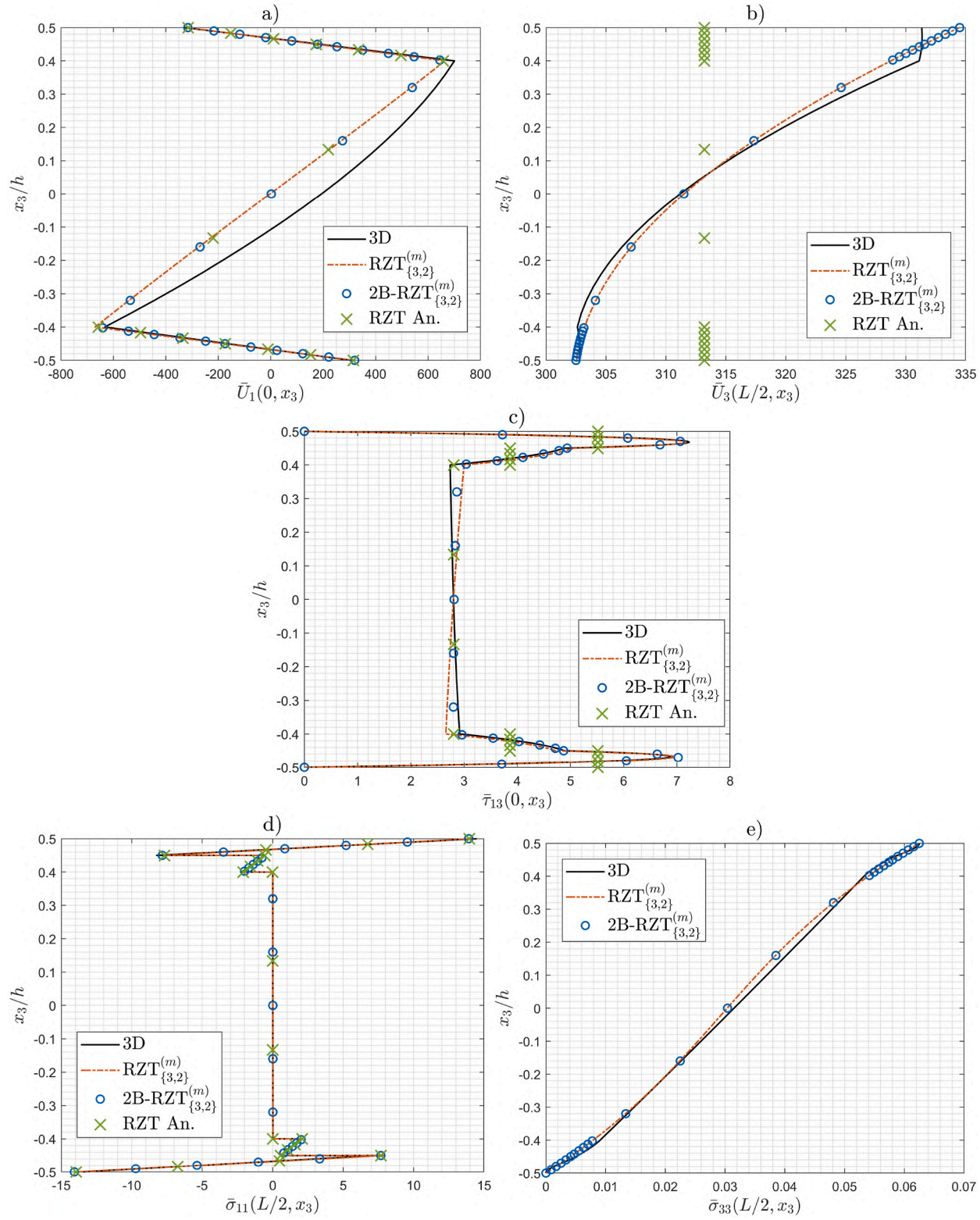

Fig. 5. Through-the-thickness distributions of normalised displacements (a–b) and stresses (c–e) for a simply-supported sandwich beam (B0) under sinusoidal transverse load.

Table 4
Sandwich beam specimens nomenclature and dimensions (in mm).

Specimen ID	L	L_{eff}	b	h	h_f	L/h	h_c/h_f	L_{eff}/h
B1	640.00	600.00	90.00	44.60	3.00	14.35	12.87	13.45
B2	490.00	450.00	90.00	43.30	3.00	11.32	12.40	10.39
B3	340.00	300.00	90.00	43.50	3.00	7.82	12.50	6.90
B4	280.00	240.00	90.00	43.10	3.00	6.50	12.37	5.57

Table 5
Experimental mechanical properties. Young's and shear modulus are in MPa.

Material	E	G
EN-AW 7075 T6 (Ergal)	67545	25393
Rohacell® IG-31[a]	43.2 ± 2.0	12.1

[a] in the transverse direction, the compressive modulus is considered (E = 17 MPa), see Ref. [57].

the following comparisons between the experimental and the new numerical model results.

5.2. Sensors, acquisition system and numerical models

One of the novelty aspects of this experimental assessment is measuring the strains at both layer interfaces between the IG-31 core and the Ergal Aluminium face-sheets. The Distributed Fibre Optic Strain (DFOS) sensors have been produced in-house by the Department of Aerospace Sciences and Technologies at Politecnico di Milano and embedded in the sandwich layup during manufacturing. The DFOS sensors are placed parallel to the beam's longitudinal axis according to the configuration scheme reported in Fig. 6.

Moreover, a groove guide on both the Ergal face-sheet has been added to keep the sensor in position during the curing process, and subsequently, when the adhesive layer is placed, as shown in Fig. 7a. Finally, the bonding process and the following cure process have been performed in the autoclave. Then, the sandwich beams were placed in a mechanical press to restore the planarity between the Ergal face-sheets, modified due to the protecting supports for the optic fibre sensors, see Fig. 7b.

In addition to the DFOS sensors, some strain gauges were placed on the outer beam surfaces. Four strain gauges, here denoted with the labels E1, E2, E3 and E4, were placed for each beam, two on top and two on bottom surfaces, to measure the axial strains. A further strain gauge (E5) has been placed to verify the symmetry of the supporst and of the applied loading conditions during the test. The transverse displacements at the top and bottom surfaces have been measured using three LVDTs. Two have been positioned where the force is applied (W1 and W2), and the third is positioned on the bottom surface at the centre of the beam (W3). The load cell, LVDTs and strain gauges positioned on the beam specimen are shown in Figs. 8 and 9.

Two semi-circular cylinders are used to provide the supported boundary conditions for the three- and four-point bending tests, Fig. 10. The supported boundary condition typically adopted in numerical models prescribes a null transverse displacement on the supported edge and no transverse normal deformability is allowed along the whole cross-section. However, in this experimental assessment, the supported conditions are modelled differently in both $2B-RZT^{(m)}_{\{3,2\}}$ and NASTRAN models. The vanishing condition on the transverse displacement has been enforced only on the contact point between the beam specimen and the supporting cylinder, i.e. on the bottom beam surface, as follows:

$$\begin{aligned} &@x_1 = -\frac{L_{eff}}{2}, +\frac{L_{eff}}{2} \qquad U_3\left(x_3 = x_{3(B)}\right) = 0 \\ &@x_1 = 0 \qquad\qquad U_1^{(k)}(x_3) = 0 \rightarrow u = 0, \theta = 0, \psi = 0 \end{aligned} \tag{45}$$

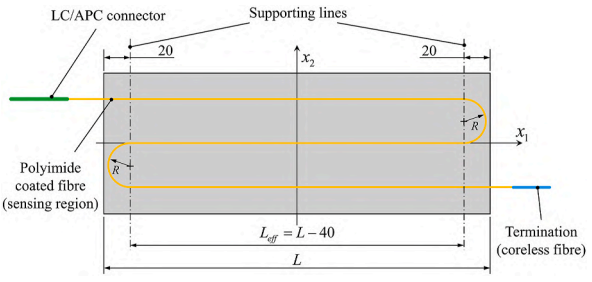

Fig. 6. Sensor components and top-view of the DFOSs positioning at the interface (data are given in mm, R = 15 mm).

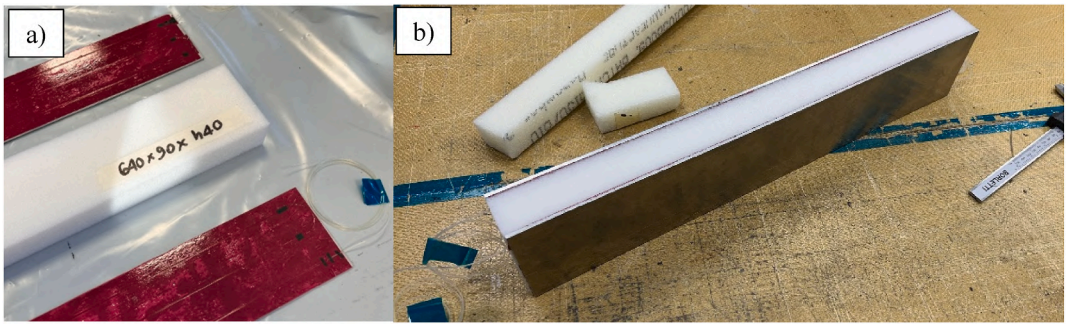

Fig. 7. a) Details of DFOSs placed on the Ergal face-sheets, adhesive layer (in red) and Rohacell® IG-31 foam; b) final manufactured sandwich specimen (B2) after mechanical pressing.

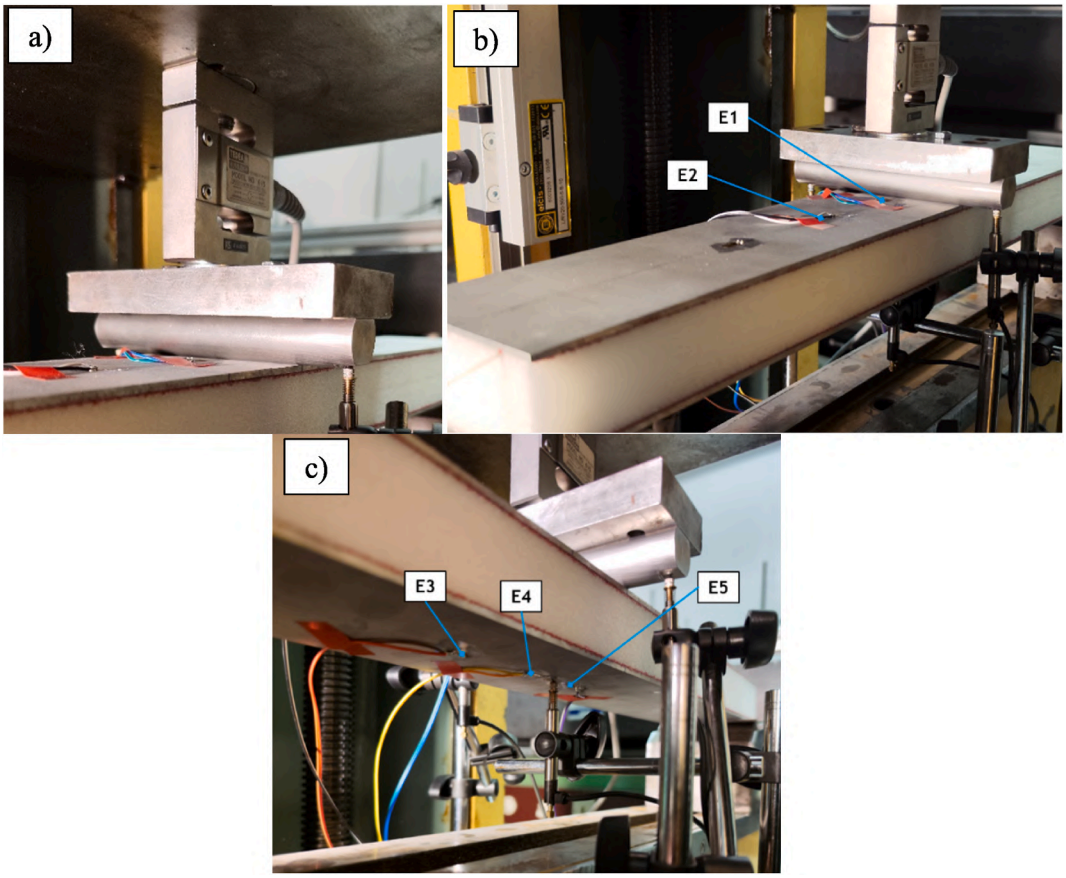

Fig. 8. a) HBM strain gauge load cell (200 kg); strain gauges on beam top (b) and bottom (c) surfaces.

Note that in Eq. (45), a further condition on the axial displacement has been enforced on the mid-span point (symmetry condition).

For comparison purposes, alongside the 2B − $\text{RZT}^{(m)}_{\{3,2\}}$ and NASTRAN models, the Timoshenko-based elements (TIM), typically implemented in the FE commercial codes, are included in this numerical-experimental assessment. The TIM elements selected to discretize the sandwich beams are the simple linear Lagrangian two-node elements (with full integration). To better estimate the transverse shear deformability, a shear correction factor was computed using the Raman-Davalos methodology [58]. The values for each beam specimen are as follows: B1: 0.25732; B2: 0.25009; B3: 0.25120; B4: 0.24898.

The beam models adopt a discretization using 0.5 mm 2B − $\text{RZT}^{(m)}_{\{3,2\}}$ and TIM elements for each specimen. Concerning the 2D high-fidelity NASTRAN FE model, each sandwich is discretised using membrane QUAD4 elements able to simulate the beam flexural beahviour in the plane (x_1, x_3). To achieve a good numerical representation of the bending beahviour, in the NASTRAN FE model, the

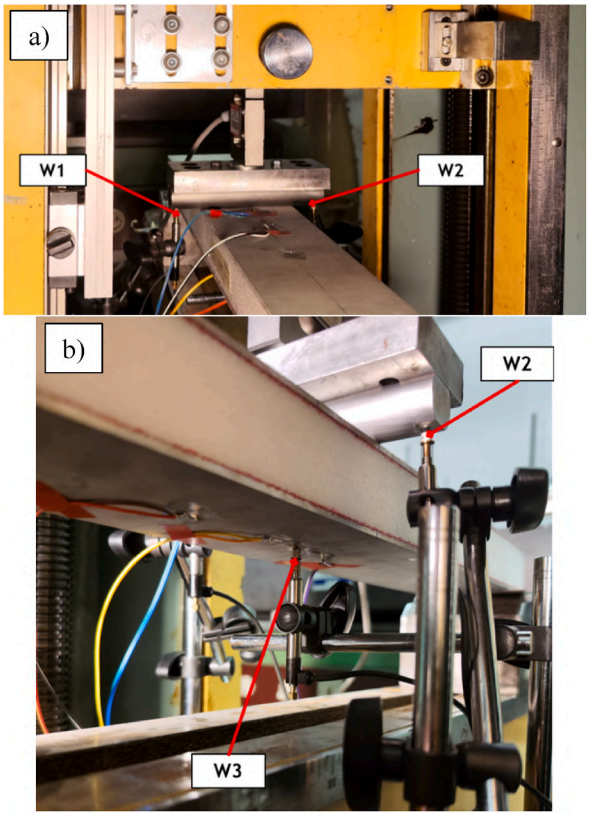

Fig. 9. LVDTs positioning and nomenclature for the top (a) and bottom (b) transverse displacements.

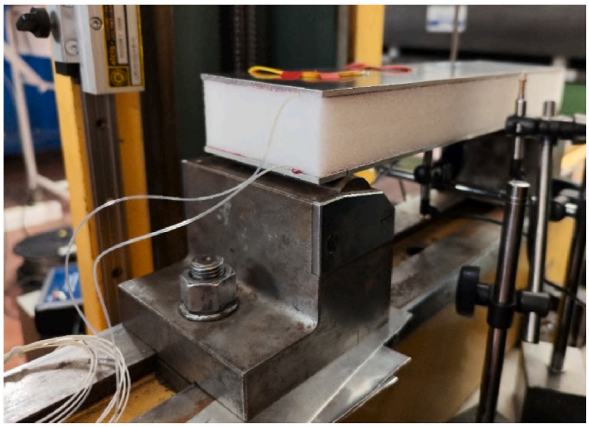

Fig. 10. Detail on the support condition for the sandwich beam specimens.

average size of the mesh is 0.25 mm. This choice of QUAD4 element size guarantees at least 170 elements along the thickness direction, which is useful to evaluate the transverse normal deformability in x_3 direction. Within the aim to limit the computational cost of the NASTRAN FE model, the symmetry boundary conditions are adopted on the sandwich beams' mid-span. In both NASTRAN, TIM and $2B-\mathrm{RZT}^{(m)}_{\{3,2\}}$ FE models, the effect of the adhesive layer is considered. Due to the difficulty in measuring the adhesive layer thickness, its value is considered constant along the beam length and equal to 0.25 mm, i.e. the nominal value taken from the producer datasheet (see, Ref. [55]). For this reason, in both numerical models, the effective core thickness is the measured one subtracted by the sum of the thickness of the two adhesive layers. In order to investigate the response even in the region closer to the supports, the span of the sandwich beam outside the supports is modelled in both NASTRAN, TIM and $2B-\mathrm{RZT}^{(m)}_{\{3,2\}}$ FE models.

Table 6 reports the number of elements, the corresponding total dofs and the mesh discretisations for the sandwich beam models.

Table 6
Number of elements, dofs and mesh discretization in $2B-RZT^{(m)}_{\{3,2\}}$, TIM and NASTRAN models for static analysis. In the NASTRAN mesh, the first number is the element discretization along the x_1 direction, the second one is the discretization in the x_3 direction.

Beam ID	TIM		$2B-RZT^{(m)}_{\{3,2\}}$		NASTRAN		
	N_e	Total dofs	N_e	Total dofs	Mesh	Total number of elements	Total dofs
B1	1280	3843	1280	7686	1280 x 178	227840	458458
B2	980	2943	980	5886	980 x 173	169540	341388
B3	680	2043	680	4086	680 x 174	118320	236640
B4	560	1683	560	3366	560 x 172	96320	194106

The entire sandwich beams are discretised using TIM or $2B-RZT^{(m)}_{\{3,2\}}$ FE elements. The same BCs given in Eq. (45) are applied to the TIM FE models, with the expection of the varible ψ, that is not present in Timoshenko beam theory. Specifically, no boundary conditions are applied on the strain dofs for $2B-RZT^{(m)}_{\{3,2\}}$.

5.3. Three- and four-point bending test configurations

The three- and four-point bending tests are performed according to the scheme given in Figs. 11 and 12, respectively. The nomenclature for the transverse displacements and strains is also reported in Figs. 11 and 12. The experimental axial strains are also evaluated across the thickness-wise direction, specifically at each layer interface in two beam sections $x_{S1} = -20$ mm and $x_{S2} = -75$ mm. The position of strain gauge E5 used to evaluate the symmetry condition of the load-supports configuration is $x_1 = +20$ mm.

The measured axial strains along the axial coordinate of the three rectilinear lines of the DFOS sensors are averaged to obtain a single strain function representative of the cylindrical bending beam behaviour. The reason is dictated by the high resolution of the optic fibre sensors that are very sensitive to geometry imperfections.

The tests were performed by increasing the applied load and reaching four different load levels to measure the quantities appropriately and verifying the linearity between applied force intensity and displacement/strain data for each beam specimen.

5.4. Experimental-numerical comparison

After validating numerically the accuracy of the proposed $RZT^{(m)}_{\{3,2\}}$ model, the results obtained by the experimental campaign are resumed and compared with the numerical results using the $2B-RZT^{(m)}_{\{3,2\}}$ and TIM elements and, for axial strain distribution, also with 2D high-fidelity NASTRAN model. The following presented results concerning transverse displacements and axial strains are normalised with respect to the force intensity, taking advantage of the linearity of the problem.

5.4.1. Three-point bending case

Table 7 compares the experimental normalised displacements and those computed using the $2B-RZT^{(m)}_{\{3,2\}}$ and TIM models. Moreover, in brackets the percent errors of the numerical solution with respect to the experimental one are also reported. The transverse displacement positions correspond to the three-point bending scheme shown in Fig. 11.

From Table 7 it is observed that in most cases, the percent errors of $2B-RZT^{(m)}_{\{3,2\}}$ are bounded in the 10 %, which is quite acceptable for an experimental assessment. However, for sandwich beam B3, the discrepancies in the bottom and top transverse displacements exceed 10 % due to the uncertainties in the IG-31 foam core characterisation, which is quite sensible to the mechanical pressisng phase during the beam manufacturing process. As expected, the TIM FE model, even with the shear correction factor considered, underestimates the transverse maximum deflection, since its formulation does not take into account the transverse normal deformability present in thick sandwich structures and provides an inaccurate evaluation of the transverse shear deformability due to the high

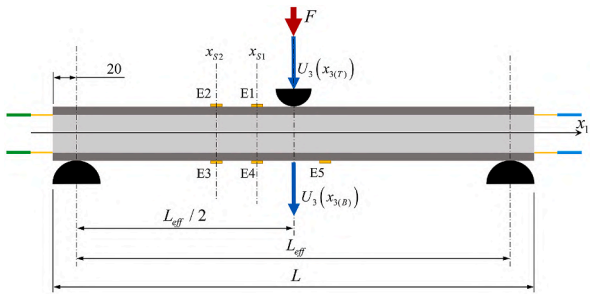

Fig. 11. Scheme for three-point bending test and nomenclature for strain gauges and displacements (in mm).

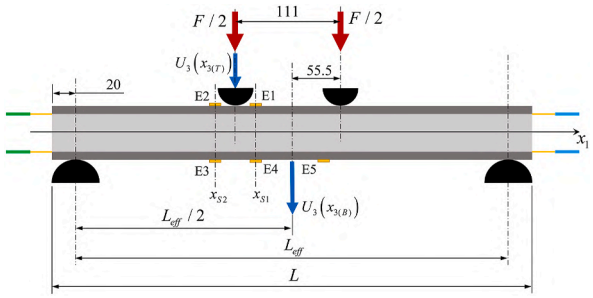

Fig. 12. Scheme for four-point bending test and nomenclature for strain gauges and displacements (in mm).

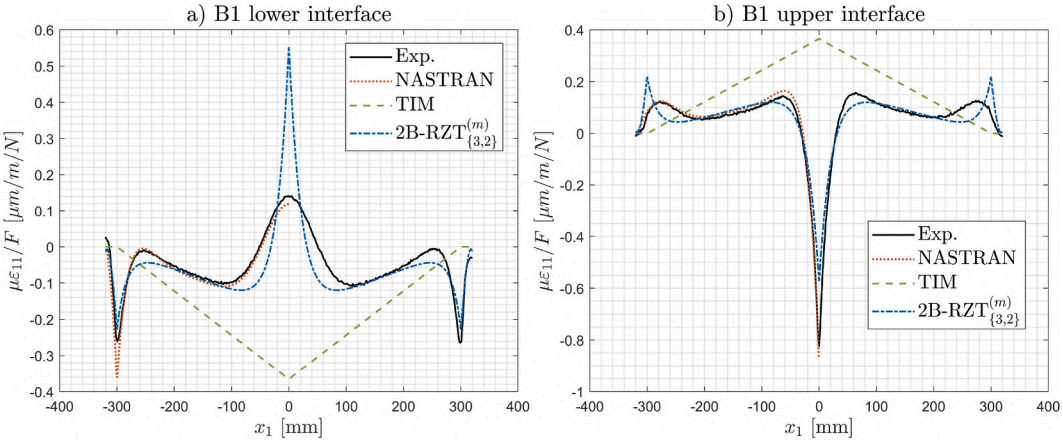

Fig. 13. Axial strain distributions along the longitudinal axis for beam B1 at a) lower and b) upper interfaces between core and Ergal face-sheets (three-point bending).

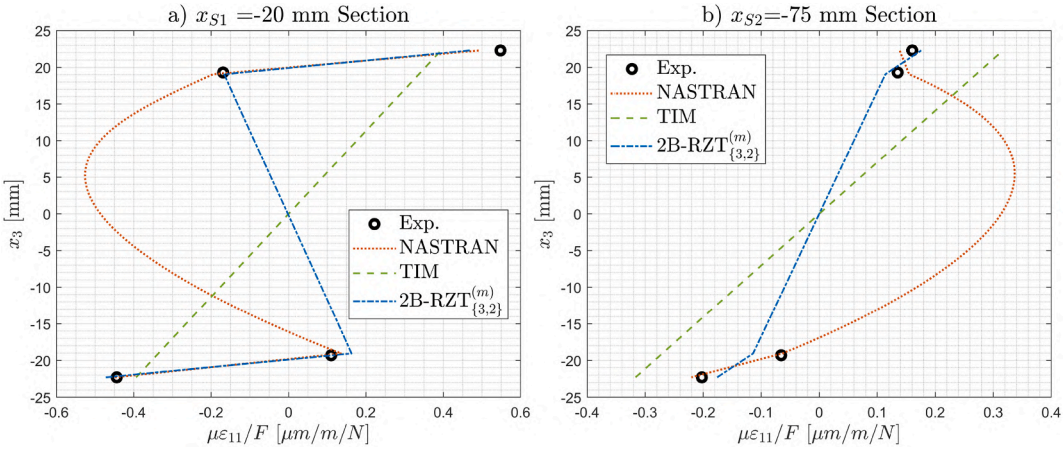

Fig. 14. Through-the-thickness distribution of axial strains in two beam sections (a–b) for beam B1 (three-point bending).

transverse anisotropy.

Figs. 13, 15, 17 and 19 report the axial strain distributions at the lower and upper interfaces between the core layer and the Ergal face-sheets. The longitudinal strains at the sandwich interfaces are observed experimentally and compared with the numerical results for the first time. The effect of concentrated forces and boundary conditions are observable as spikes in the strain distributions along the beam axis.

As expected, the high-fidelity NASTRAN FE model can follow the experimental data. However, even though the 2B– RZT$^{(m)}_{\{3,2\}}$ FE model can follow the experimental strain distributions, some spikes in the numerical axial strains are observable in the correspondence

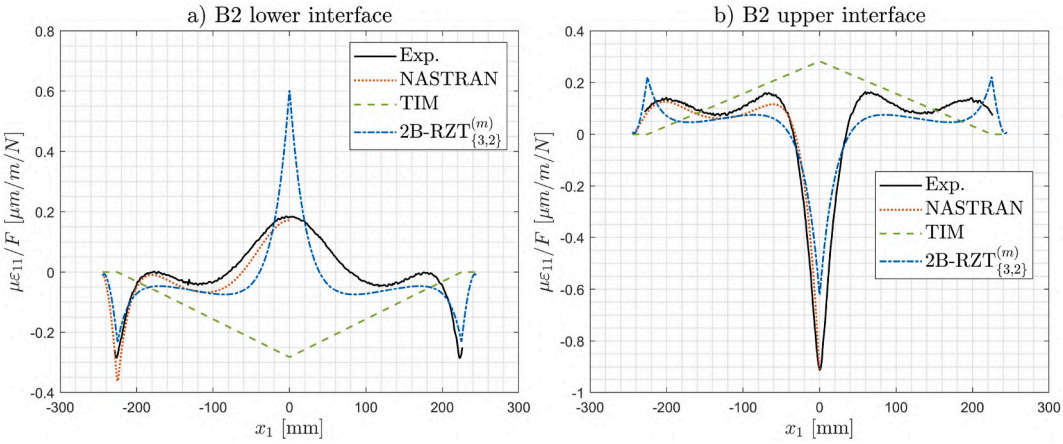

Fig. 15. Axial strain distributions along the longitudinal axis for beam B2 at a) lower and b) upper interface between core and Ergal face-sheets (three-point bending).

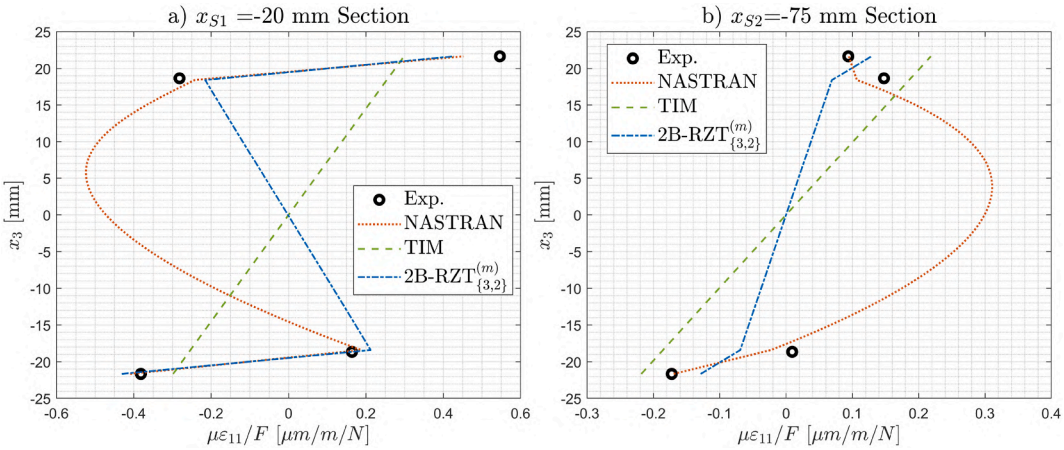

Fig. 16. Through-the-thickness distribution of axial strains at two beam sections (a–b) for beam B2 (three-point bending).

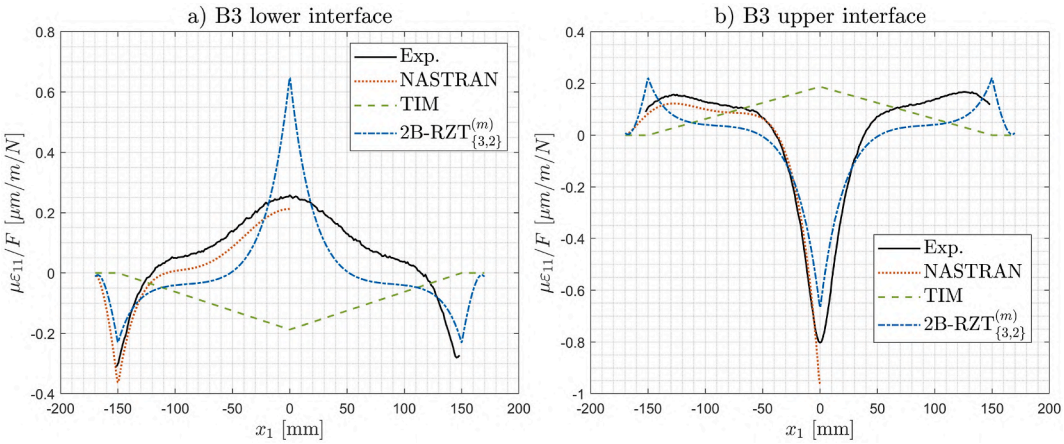

Fig. 17. Axial strain distributions along the longitudinal axis for beam B3 at a) lower and b) upper interface between core and Ergal face-sheets (three-point bending).

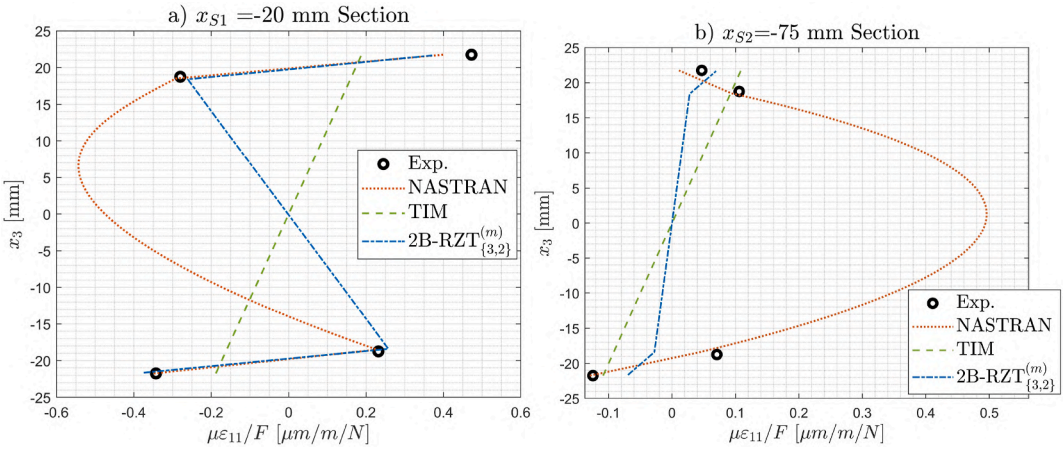

Fig. 18. Through-the-thickness distribution of axial strains at two beam sections (a–b) for beam B3 (three-point bending).

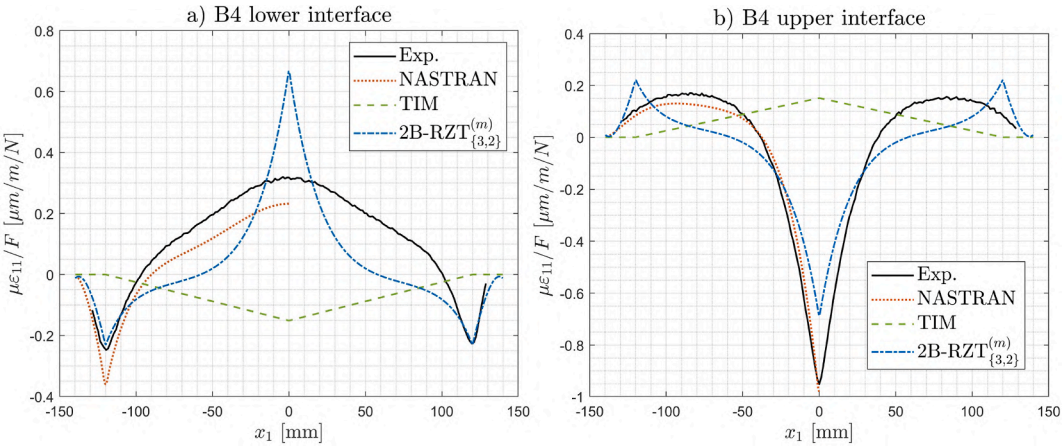

Fig. 19. Axial strain distributions along the longitudinal axis for beam B4 at a) lower and b) upper interfaces between core and Ergal face-sheets (three-point bending).

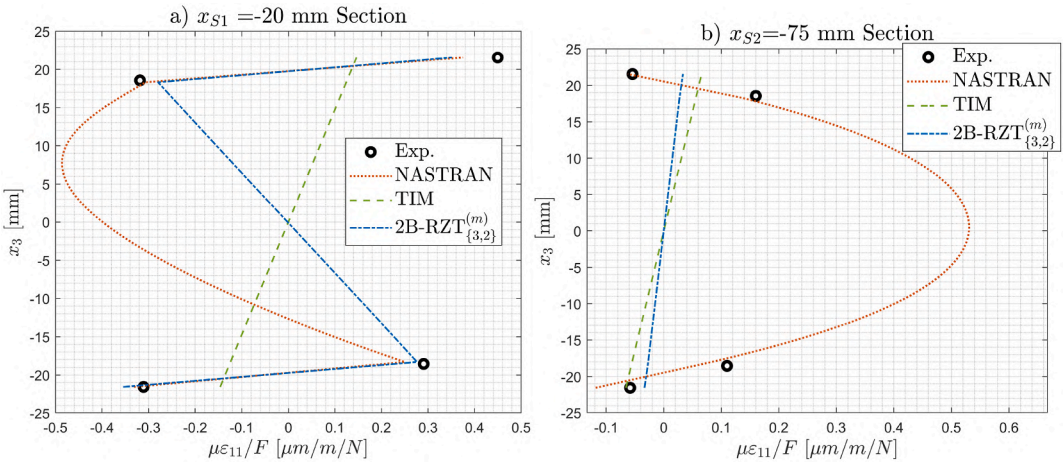

Fig. 20. Through-the-thickness distribution of axial strains at two beam sections (a–b) for beam B4 (three-point bending).

of the applied force and supported boundary conditions. The results obtained using the Timoshenko (TIM) beam elements are very far from the real beam beahviour, which makes the $2B-RZT^{(m)}_{\{3,2\}}$ elements more accurate in predicting the strain distributions.

Figs. 14, 16, 18 and 20 report the through-the-thickness distributions of the normalised axial strains across the two beam cross-sections located at $x_{S1} = -20$ mm and $x_{S2} = -75$ mm. For the first time it can be observable experimentally the typical "zigzag" distribution of axial strains in a sandwich multilayered structure. As expected, the numerical data computed from the high-fidelity NASTRAN FE model are quite closer to those determined experimentally for each beam specimen. Even the $2B-RZT^{(m)}_{\{3,2\}}$ estimates correctly the strain values at both interfaces for x_{S1} section, whereas higher discrepancies are visible in x_{S2} section. A reasonable explanation is the limitation of the $2B-RZT^{(m)}_{\{3,2\}}$ elements and, in more generally, the $RZT^{(m)}_{\{3,2\}}$ model to predict more complex distributions of the transverse normal stress. The third-power series expansion assumed here could not be sufficiently accurate to describe the sandwich behaviour in some particular beam regions, such as near concentrated loads or in core regions with a transverse normal deformability that influences the axial strain distribution, e.g. for three-point bending the x_{S2} section. Despite these concers, the TIM elements cannot reach the same level of accuracy given by the zigzag model in through-the-thickness axial strain distribution, as demonstrated in Figs. 14, 16, 18 and 20.

In order to better evaluate the role of the concentrated loads in the numerical FE predictions, a slightly different numerical load configuration has been considered for beam B01. In this example, a distributed load equivalent to the concentrated force is applied on the upper surface of the sandwich beam for a length of 1 mm, at the same point of the three-point load configuration. Note that the same discretization adopted in Table 6 for beam B1 has been used to guarantee that the load is correctly distributed, i.e. a mesh with 1280 $2B-RZT^{(m)}_{\{3,2\}}$ elements. In Table 8 are reported, for comparison purposes with the previous numerical $RZT^{(m)}_{\{3,2\}}$ results, the transverse displacements at the beam mid-span, evaluated at the top and bottom surfaces.

Table 8 reports a slightly improvement in predicting the central transverse displacement using the $2B-RZT^{(m)}_{\{3,2\}}$ elements in the second load configuration case (distributed load). However, the same numerical improvement is not obtained for the axial strain distributions, as reported by Fig. 21.

As observable in Fig. 21, the strain distributions obtained considering a localized distributed load are almost identical with those computed by considering a concentrated force. However, by taking a closer look at the region closer to the beam mid-length, the strains corresponding to the previous numerical model, i.e. that with the concentrated force, are better evaluated than those obtained with the equivalent distributed load. In addition, the localised distributed force in the second numerical model shows an abrupt slope change in the resulting strains which is not observed in the experimental data.

Although, some improvements in the numerical predictions are observed from a global point of view, e.g. transverse displacements, a worsening effect has observed for the strain distributions. Thus, as a results of these considerations, the numerical model with concentrated forces is adopted for the four-point bending analysis.

5.4.2. *Four-point bending*

Table 9 compares the experimental normalised transverse displacements and those computed using the $2B-RZT^{(m)}_{\{3,2\}}$ model for the four-point bending configuration, as reported in Fig. 12.

As shown in Table 9 for the four-point bending configuration, the transverse displacements obtained by the $2B-RZT^{(m)}_{\{3,2\}}$ FE model are closer to the experimental data, with errors bounded in +2.4/-10 %. In fact, for such load configuration, the force is not localised in one single point, such as the three-point bending scheme, but it is divided into two separated points that distribute differently the effect of the transverse normal deformability in the beam specimens. The $2B-RZT^{(m)}_{\{3,2\}}$ still confirm its superior predictive capabilities for the transverse displacements with respect to the TIM FE model, for each sandwich beam.

Figs. 22, 24, 26 and 28 report the axial strain distributions at the lower and upper interfaces between the core layer and the Ergal face-sheets for the four-point bending case. The numerical results confirm the previous considerations. The high-fidelity NASTRAN FE model is able to follow the experimental strain distributions along the beam axis at the inner sandwich beam interfaces; the discrepancies observable are due to the uncertainties in the correct estimation of the IG-31 material properties probably caused by the manufacturing process, e.g. mechanical pressing phase. The results provided by the $2B-RZT^{(m)}_{\{3,2\}}$ FE model are generally able to follow

Table 7
Normalised displacements (in mm/N) for three-point bending test: experimental and numerical values, in brackets the percent errors.

Beam specimen ID	Normalised transverse displacements	Experimental values	**2B**-$RZT^{(m)}_{\{3,2\}}$	TIM
B1	$U_3(x_{3(T)})/F$	3.354E-03	3.601E-03 (7.4)	6.527E-04 (−80.5)
	$U_3(x_{3(B)})/F$	3.009E-03	2.913E-03 (−3.2)	6.527E-04 (−78.3)
B2	$U_3(x_{3(T)})/F$	2.891E-03	2.737E-03 (−5.3)	3.207E-04 (−88.9)
	$U_3(x_{3(B)})/F$	2.269E-03	2.051E-03 (−9.6)	3.207E-04 (−85.9)
B3	$U_3(x_{3(T)})/F$	2.283E-03	1.865E-03 (−18.3)	1.183E-04 (−94.8)
	$U_3(x_{3(B)})/F$	1.713E-03	1.178E-03 (−31.2)	1.183E-04 (−93.1)
B4	$U_3(x_{3(T)})/F$	1.589E-03	1.544E-03 (−2.9)	7.412E-05 (−95.3)
	$U_3(x_{3(B)})/F$	1.062E-03	8.571E-04 (−19.3)	7.412E-05 (−93.0)

Table 8
Normalised displacements (in mm/N) for three-point bending test: experimental and numerical values for concentrated and distributed load (in brackets the percent errors).

Beam specimen ID	Normalised transverse displacements	Experimental values	**2B**-RZT$^{(\mathbf{m})}_{\{3,2\}}$	
			Concentrated force (see, Table 7)	Distributed load
B1	$U_3(x_{3(T)})/F$	3.354E-03	3.601E-03 (7.4)	3.504E-3 (4.5)
	$U_3(x_{3(B)})/F$	3.009E-03	2.913E-03 (−3.2)	2.956E-3 (−1.8)

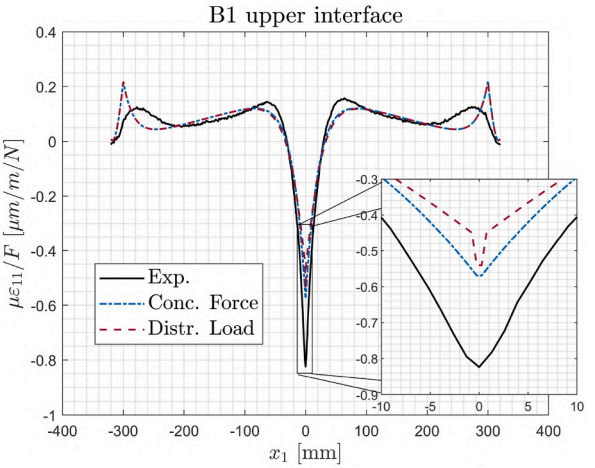

Fig. 21. Comparison of axial strain distributions along the upper interface of sandwich specimen B1.

Table 9
Normalised displacements (in mm/N) for four-point bending test: experimental and numerical values, in brackets the percent errors.

Beam specimen ID	Normalised transverse displacements	Experimental values	**2B**-RZT$^{(\mathbf{m})}_{\{3,2\}}$	TIM
B01	$U_3(x_{3(T)})/F$	2.881E-03	2.938E-03 (2.0)	5.869E-04 (−79.6)
	$U_3(x_{3(B)})/F$	2.886E-03	2.858E-03 (−1.0)	6.103E-04 (−78.9)
B02	$U_3(x_{3(T)})/F$	2.238E-03	2.070E-03 (−7.5)	2.664E-04 (−88.1)
	$U_3(x_{3(B)})/F$	2.050E-03	1.991E-03 (−2.9)	2.837E-04 (−86.2)
B03	$U_3(x_{3(T)})/F$	1.334E-03	1.209E-03 (−9.4)	7.954E-05 (−94.0)
	$U_3(x_{3(B)})/F$	1.226E-03	1.125E-03 (−8.2)	8.911E-05 (−92.7)
B04	$U_3(x_{3(T)})/F$	9.176E-04	8.907E-04 (−2.9)	4.096E-05 (−95.5)
	$U_3(x_{3(B)})/F$	7.857E-04	8.047E-04 (2.4)	4.764E-05 (−93.9)

the experimental strain distribution with the expected differences due to the assumed transverse stress distribution. Moreover, considering the upper beam interfaces, the 2B − RZT$^{(m)}_{\{3,2\}}$ model can match the experimental strain spikes that appear in the strain distribution where the concentrated forces are applied. On the other hand, the 2B − RZT$^{(m)}_{\{3,2\}}$ FE models the same experimental strain spikes in correspondence of the supporting cylinder at the lower sandwich interfaces. Even in this case, the Timoshenko model fails to predict the axial strain distributions at the layer interfaces when compared to the high-fidelity solution and the experimental results. The TIM results differ not only in magnitude but also in sign, making them less accurate from the 2B − RZT$^{(m)}_{\{3,2\}}$ predictions.

However, the numerical strain values provided by the 2B − RZT$^{(m)}_{\{3,2\}}$ are relatively close to the experimental ones, as reported in Figs. 23, 25, 27 and 29. It is particularly interesting, in the four-point bending tests, that the 2B − RZT$^{(m)}_{\{3,2\}}$ is able to predict the experimental "zigzag" pattern of the through-the-thickness axial distribution, evaluating correctly the extreme values and slopes for the strains in the Aluminium face-sheets in the slender sandwich beam specimen, i.e. B1. As expected, the TIM FE results for top and bottom strain values are very different from those experimentally observed, and confirm the superior accuracy of the 2B− RZT$^{(m)}_{\{3,2\}}$ elements.

From the presented results it appears quite clear the inherent complexity behind the experimental study of thick sandwich beams characterised by a soft core, such as the IG-31, that exhibits a pronounced transverse normal deformability. Moreover, the higher discrepancies between experimental and numerical results, especially for beam B3, are probably due to the uncertainties of the

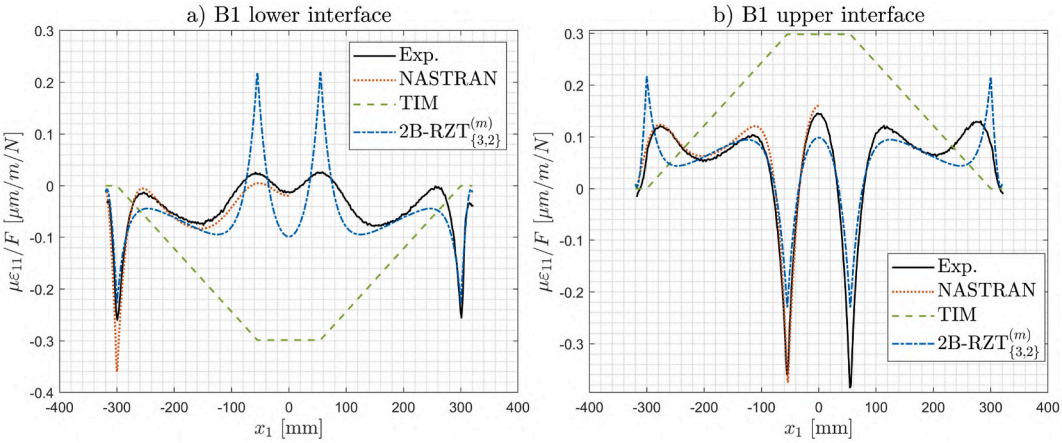

Fig. 22. Axial strain distributions along the longitudinal axis for beam B1 at a) inferior and b) superior interface between core and Ergal face-sheets (four-point bending).

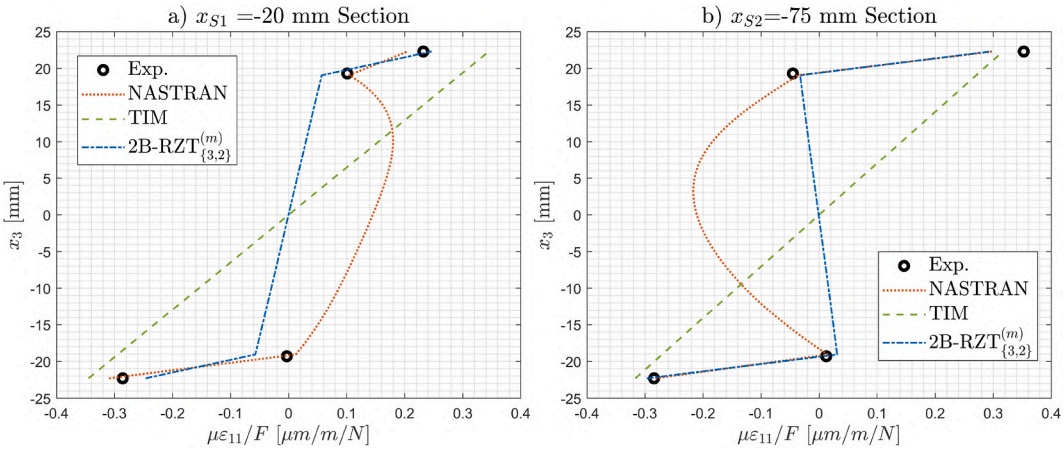

Fig. 23. Through-the-thickness distribution of axial strains at two beam sections for beam B1 (four-point bending).

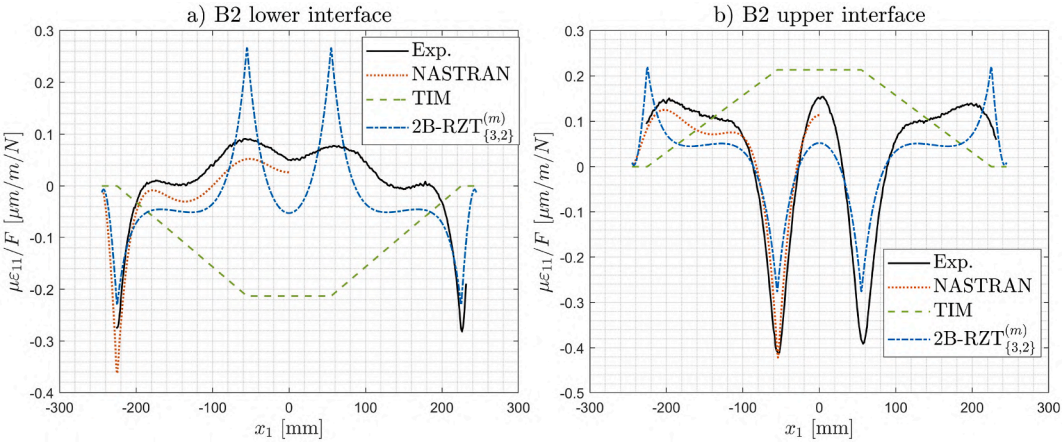

Fig. 24. Axial strain distributions along the longitudinal axis for beam B2 at a) inferior and b) superior interface between core and Ergal face-sheets (four-point bending).

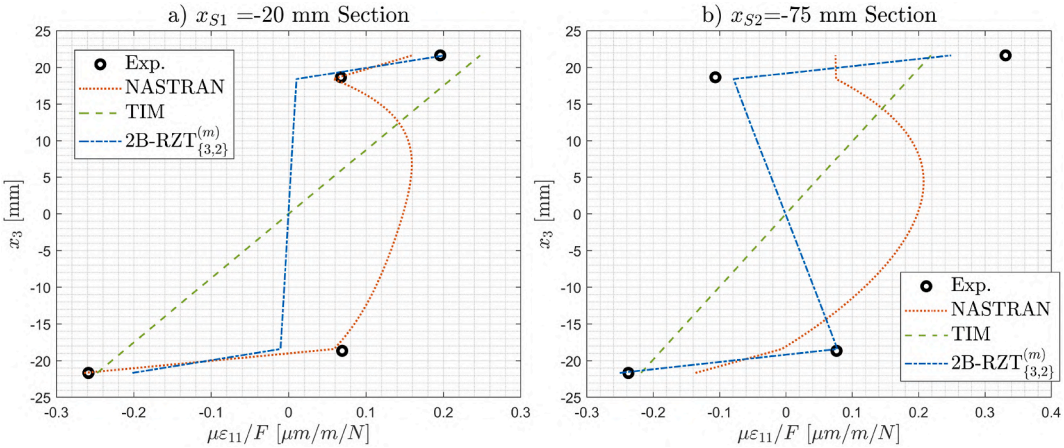

Fig. 25. Through-the-thickness distribution of axial strains at two beam sections for beam B2 (four-point bending).

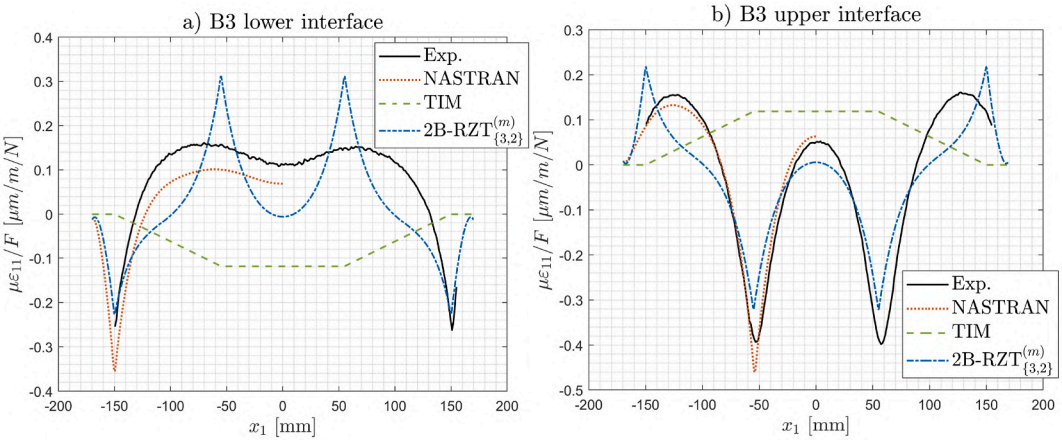

Fig. 26. Axial strain distributions along the longitudinal axis for beam B3 at a) inferior and b) superior interface between core and Ergal face-sheets (four-point bending).

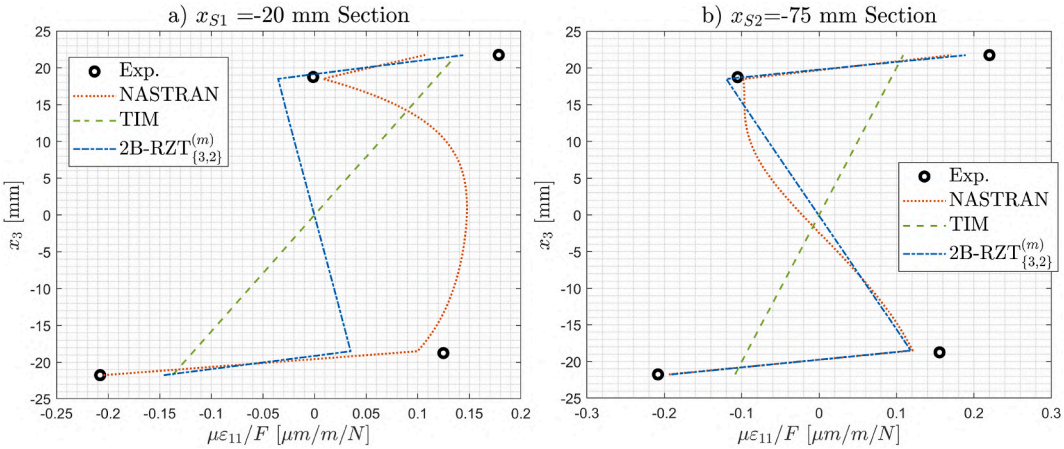

Fig. 27. Through-the-thickness distribution of axial strains at two beam sections for beam B3 (four-point bending).

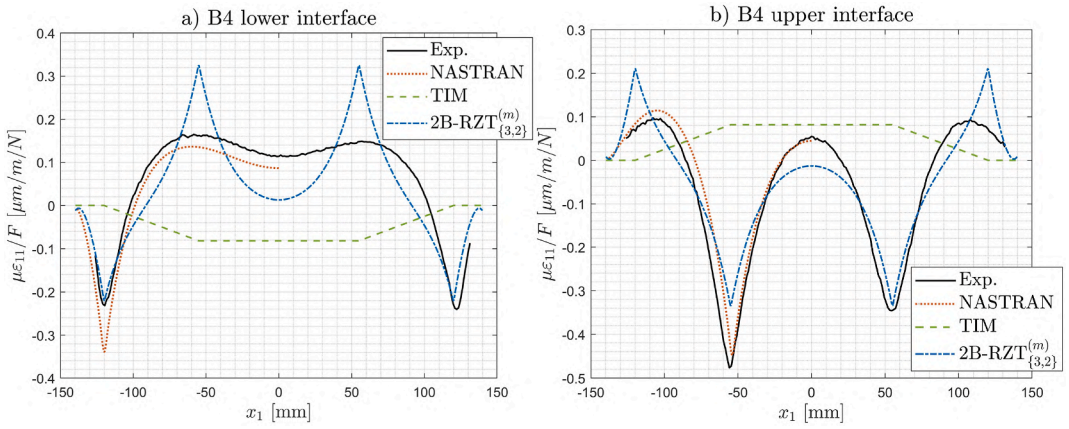

Fig. 28. Axial strain distributions along the longitudinal axis for beam B4 at a) inferior and b) superior interface between core and Ergal face-sheets (four-point bending).

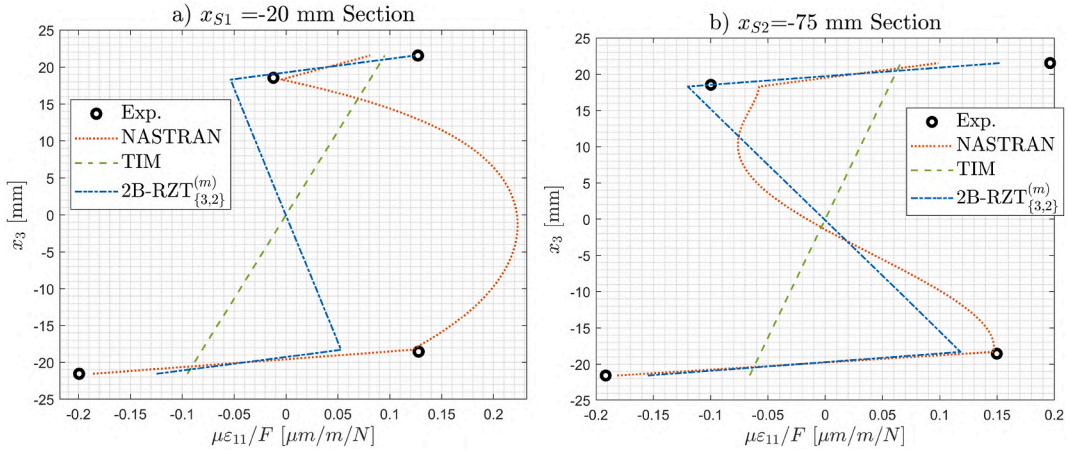

Fig. 29. Through-the-thickness distribution of axial strains at two beam sections for beam B4 (four-point bending).

material foam core characterisation. Clearly, a more detailed material characterisation that considers the degradation of the material properties (Young's modulus in the transverse direction) due to the manufacturing process (e.g. mechanical pressing phase) could lead to a more realistic modelisation of these sandwich specimens. These last considerations suggest a possible explanation for the discrepancies observed in the predicted numerical axial strain distributions in some core regions closer to the concentrated loads.

Generally speaking, experimental data for strain values determined for thick sandwich structures are rarely found in the current literature, and further efforts to improve the accuracy of the transverse normal deformability are suggested in the future.

6. Conclusions

The paper presents an experimental campaign performed to assess the new mixed {3,2}-RZT beam model, i.e. RZT$^{(m)}_{\{3,2\}}$. The kinematic assumptions, the assumed stress fields, the governing equations, and the consistent boundary conditions of the RZT$^{(m)}_{\{3,2\}}$ model are derived using a mixed variational statement based on the Hellinger-Reissner functional and on a penalty functional to enforce the strain compatibilities. In virtue of the C^0-continuity requirements, the linear Lagrangian shape functions are adopted to formulate a simple low-order two-node beam element. Static condensation has been used at the element level to reduce the number of dofs. A first numerical assessment has been performed to evaluate the accuracy of the present theory and formulated element to predict the through-the-thickness quantities correctly for simply-supported sandwich beams with transverse load configuration. The results demonstrate the present formulation's accuracy in addressing the sandwich behaviour compared with the exact three-dimensional solution.

A set of four thick sandwich beam specimens with different length-to-thickness ratios are manufactured. Each beam is made of two 7075 Aluminium alloy face-sheets (Ergal), whereas the core layer is made of soft foam Rohacell® IG-31. Each specimen is equipped with Distributed Fibre Optic Strain (DFOS) sensor embedded at each layer interface. Furthermore, the beam deflection is measured at

two different positions, and the axial strains are evaluated in two different sections on the outer beam surfaces.

The experimental campaign's first phase is dedicated to material characterisation. Then, three- and four-point bending tests are conducted for each beam specimen, evaluating the transverse deflections and axial strains. The experimental results are compared with those coming from the $2B-\mathrm{RZT}^{(m)}_{\{3,2\}}$ and TIM FE models and those from a high-fidelity NASTRAN FE model.

Thanks to the DFOS sensors embedded in the sandwich beam layup, it has been possible to measure the axial strains at the inner interfaces and compare them with the available numerical models. The $2B-\mathrm{RZT}^{(m)}_{\{3,2\}}$ FE model is able to accurately predict the expected spikes in the axial strain distributions in the correspondence points of concentrated forces and/or supported boundary conditions. On the contrary, the TIM model cannot correctly estimate the axial strain distributions, even with the use of an appropriate shear correction factor. Additionally, the TIM fails also in predicting the transverse displacement quantities with respect to the experimental results.

For the first time, the typical "zigzag" through-the-thickness distributions of the axial strains it has been observed experimentally in for three- and four-point test configurations, confirming the accuracy of the developed $2B-\mathrm{RZT}^{(m)}_{\{3,2\}}$ model in predicting the strain quantities at the inner and outer interfaces for the slender beam case. These results also confirm the superior capabilities of the RZT-based models over the Timoshenko one, in represent the through-the-thickness strain distributions for thick structures with higher accuracy. As observed by the experimental-numerical comparisons, this set of sandwich beam specimens exhibits a more pronounced transverse normal deformability when concentrated forces are applied, mainly due to the soft foam core material adopted in the stacking sequences and material property degradation in the transverse direction. For this reason, the assumed distribution of the transverse normal stress in the $\mathrm{RZT}^{(m)}_{\{3,2\}}$ model could exhibit higher discrepancies with respect to the real one.

The paper aims to present a new set of experimental data for thick sandwich structures in which the transverse deformability is not negliglibe and influences the overall sandwich static response. The present mixed-model formulation offers an advantageous methodology for formulating accurate and computational efficient simple beam finite elements for the analysis of thick sandwich structures. Additionally, the mixed-formulation via the Hellinger-Reissner functional has demonstrated to achieve better results for transvese shear and normal stress distributions without recurring to the *a-posteriori* stress-recovery typical of the PVDs-formulated elements. However, the assumptions for the third-order zigzag and the transverse normal stress distributions still limit a finer description of the thick sandwich response under concentrated forces. Future steps will be dedicated to considering a more accurate description of the transverse normal deformability, more compatible with those encountered in sandwich configurations and capable to address the trough-the-thickness material change.

Fundings

This research received no specific grant from any funding agency in the public, commercial, or not-for-profit sectors.

CRediT authorship contribution statement

M. Sorrenti: Writing – original draft, Visualization, Validation, Software, Methodology, Investigation, Data curation, Conceptualization. **M. Gherlone:** Writing – review & editing, Validation, Supervision, Resources, Project administration, Funding acquisition, Formal analysis.

Declaration of competing interest

The authors declare that they have no known competing financial interests or personal relationships that could have appeared to influence the work reported in this paper.

Data availability

Data will be made available on request.

Acknowledgement

The authors would like to thank Prof. Daniela Rigamonti and Prof. Paolo Bettini of the Department of Aerospace Sciences and Technologies – DAER (Politecnico di Milano) for their support, experience and assistance in the beam manufacturing process and optic fibre sensor integration.

Appendix A. – Functions of the assumed transverse normal stress

Here are reported the through-the-thickness functions that appear in Eq. (17). These are formally the same as those obtained in Ref. [35] with the distinction that a different set of functions approximates the parabolic distribution of the transverse displacement, i.e. they differ in the definition of the $\mathbf{H}^{z}_{,3}$ term.

$$
\begin{aligned}
A^u_\sigma(x_3) &= \mathbf{P}_\sigma \langle S^{(k)}_{33} \mathbf{P}_\sigma{}^T \mathbf{P}_\sigma \rangle^{-1} \langle \mathbf{P}_\sigma{}^T R_{13}{}^{(k)} \rangle; \\
A^\theta_\sigma(x_3) &= \mathbf{P}_\sigma \langle S^{(k)}_{33} \mathbf{P}_\sigma{}^T \mathbf{P}_\sigma \rangle^{-1} \langle \mathbf{P}_\sigma{}^T R_{13}{}^{(k)} x_3 \rangle; \\
A^\psi_\sigma(x_3) &= \mathbf{P}_\sigma \langle S^{(k)}_{33} \mathbf{P}_\sigma{}^T \mathbf{P}_\sigma \rangle^{-1} \langle \mathbf{P}_\sigma{}^T R_{13}{}^{(k)} \mu^{(k)} \rangle; \\
\mathbf{A}^w_\sigma(x_3) &= \mathbf{P}_\sigma \langle S^{(k)}_{33} \mathbf{P}_\sigma{}^T \mathbf{P}_\sigma \rangle^{-1} \langle \mathbf{P}_\sigma{}^T \mathbf{H}^z_3 \rangle; \\
\mathbf{A}^{q_z}_\sigma(x_3) &= \left[\mathbf{L}_\sigma - \mathbf{P}_\sigma \langle S^{(k)}_{33} \mathbf{P}_\sigma{}^T \mathbf{P}_\sigma \rangle^{-1} \langle S^{(k)}_{33} \mathbf{P}_\sigma{}^T \mathbf{L}_\sigma \rangle \right]
\end{aligned}
\tag{A.1}
$$

Appendix B. – Functions of the assumed transverse shear stress

In this appendix, the full expression of the assumed transverse shear stress is obtained by integrating Cauchy's equation, i.e. Eq. (8), after substituting the expression of the axial stress given by Eq. (18). Integrating along the thickness direction yields

$$
\begin{aligned}
\tau^a_{13}(x_1, x_3) = &- \overline{p}_{1(B)}(x_1) + A^z(x_3) e_{,1}(x_1) + B^z(x_3) k_{,1}(x_1) + \\
&+ D^z(x_3) k^\psi_{,1}(x_1) + \mathbf{E}^{\mathbf{z}}(x_3) \partial \mathbf{w}(x_1) + \mathbf{F}^{\mathbf{z}}(x_3) \partial \overline{\mathbf{q}}_z(x_1) + \breve{a} \left(x_3 + \frac{h}{2} \right)
\end{aligned}
\tag{B.1}
$$

where, in Eq. (B.1) the through-the-thickness functions are defined as follows:

$$
\begin{aligned}
A^z(x_3) &= - \int_{-h/2}^{x_3} \left(E^{(k)}_1 + R^{(k)}_{13} A^u_\sigma \right) dx_3 \\
B^z(x_3) &= - \int_{-h/2}^{x_3} \left(x_3 E^{(k)}_1 + R^{(k)}_{13} A^\theta_\sigma \right) dx_3 \\
D^z(x_3) &= - \int_{-h/2}^{x_3} \left(E^{(k)}_1 \mu^{(k)} + R^{(k)}_{13} A^\psi_\sigma \right) dz \\
\mathbf{E}^{\mathbf{z}}(x_3) &= \left[- \int_{-h/2}^{x_3} R^{(k)}_{13} A^w_{\sigma 11} dx_3 \quad - \int_{-h/2}^{x_3} R^{(k)}_{13} A^w_{\sigma 12} dx_3 \quad - \int_{-h/2}^{x_3} R^{(k)}_{13} A^w_{\sigma 13} dx_3 \right] \\
\mathbf{F}^{\mathbf{z}}(x_3) &= \left[- \int_{-h/2}^{x_3} R^{(k)}_{13} A^{q_z}_{\sigma 11} dx_3 \quad - \int_{-h/2}^{x_3} R^{(k)}_{13} A^{q_z}_{\sigma 12} dx_3 \right]
\end{aligned}
\tag{B.2}
$$

The $\breve{a}$ term in Eq. (B.1) is obtained by enforcing the axial traction conditions at the top surface of the beam.

$$
\tau^a_{13}\left(x_1, h/2 \right) = - \overline{p}_{1(B)} - \widetilde{A} e_{,1} - \widetilde{B} k_{,1} - \widetilde{A}^\phi k^\psi_{,1} - \widetilde{\mathbf{A}}^w \partial \mathbf{w} - \widetilde{\mathbf{A}}^{qz} \partial \overline{\mathbf{q}}_z(x_1) + \breve{a} h = \overline{p}_{1(T)}
$$

It yields:

$$
\breve{a} = \frac{1}{h} \left(\overline{p}_{1(B)} + \overline{p}_{1(T)} \right) + \frac{1}{h} \widetilde{A} e_{,1} + \frac{1}{h} \widetilde{B} k_{,1} + \frac{1}{h} \widetilde{A}^\phi k^\psi_{,1} + \frac{1}{h} \widetilde{\mathbf{A}}^w \partial \mathbf{w} + \frac{1}{h} \widetilde{\mathbf{A}}^{qz} \partial \overline{\mathbf{q}}_z
\tag{B.3}
$$

Substituting Eq. (B.3) into Eq. (B.1) the complete final expression of the assumed transverse shear stress distribution is obtained:

$$
\begin{aligned}
\tau^a_{13}(x_1, x_3) = &\overline{p}_{1(B)}(x_1) \left[-1 + \frac{1}{h} \left(x_3 + h/2 \right) \right] + \frac{1}{h} \left(x_3 + h/2 \right) \overline{p}_{1(T)}(x_1) + \\
&+ \widehat{A}^z(x_3) e_{,1}(x_1) + \widehat{B}^z(x_3) k_{,1}(x_1) + \widehat{D}^z(x_3) k^\psi_{,1}(x_1) + \widehat{\mathbf{E}}^z(x_3) \partial \mathbf{w}(x_1) + \widehat{\mathbf{F}}^z(x_3) \partial \overline{\mathbf{q}}_z(x_1) = \\
&= \mathbf{Z}_p(x_3) \overline{\mathbf{q}}_\mathbf{p}(x_1) + \mathbf{Z}_t(x_3) \mathbf{q}_t(x_1) + \mathbf{Z}_{qz}(x_3) \partial \overline{\mathbf{q}}_z(x_1)
\end{aligned}
\tag{B.4}
$$

where

$$
\begin{aligned}
\widehat{A}^z(x_3) &= A^z(x_3) + \left(x_3 + h/2\right)\frac{1}{h}\widetilde{A} \\
\widehat{B}^z(x_3) &= B^z(x_3) + \left(x_3 + h/2\right)\frac{1}{h}\widetilde{B} \\
\widehat{D}^z(x_3) &= D^z(x_3) + \left(x_3 + h/2\right)\frac{1}{h}\widetilde{A}^{\phi} \\
\widehat{\mathbf{E}}^z(x_3) &= \mathbf{E}^z(x_3) + \left(x_3 + h/2\right)\frac{1}{h}\widetilde{\mathbf{A}}^{w} \\
\widehat{\mathbf{F}}^z(x_3) &= \mathbf{F}^z(x_3) + \left(x_3 + h/2\right)\frac{1}{h}\widetilde{\mathbf{A}}^{qz} \\
\mathbf{Z}_p(x_3) &= \left[-1 + \frac{1}{h}\left(x_3 + h/2\right) \quad \frac{1}{h}\left(x_3 + h/2\right)\right] \\
\mathbf{Z}_t(x_3) &= \left[\widehat{A}^z(x_3) \quad \widehat{B}^z(x_3) \quad \widehat{D}^z(x_3) \quad \widehat{\mathbf{E}}^z(x_3)\right] \\
\mathbf{Z}_{qz}(x_3) &= \widehat{\mathbf{F}}^z(x_3)
\end{aligned}
\tag{B.5}
$$

Appendix C. – Full expressions of equilibrium equation terms of $\mathrm{RZT}^{(\mathrm{m})}_{\{3,2\}}$

This appendix reports the full expressions of some terms that appear in the governing equation and boundary conditions of the $\mathrm{RZT}^{(\mathrm{m})}_{\{3,2\}}$.

$$\widehat{Q}^{w0} = -\left(\widehat{D}^{w}_{11}w^{(0)}_{,11} + \widehat{D}^{w}_{12}w^{(1)}_{,11} + \widehat{D}^{w}_{13}w^{(2)}_{,11} + \widehat{D}^{\theta}_{11}\theta_{,1} + \widehat{D}^{\psi}_{11}\psi_{,1}\right) + \widehat{A}^{kw}_{11}e_{,11} + \widehat{B}^{kw}_{11}k_{,11} + \widehat{C}^{kw}_{11}k^{\psi}_{,11} + \widehat{D}^{kw}_{11}w^{(0)}_{,11} + \widehat{D}^{kw}_{12}w^{(1)}_{,11} + \widehat{D}^{kw}_{13}w^{(2)}_{,11} \tag{C.1}$$

$$\widehat{Q}^{w1} = -\left(\widehat{D}^{w}_{11}w^{(0)}_{,11} + \widehat{D}^{w}_{12}w^{(1)}_{,11} + \widehat{D}^{w}_{13}w^{(2)}_{,11} + \widehat{D}^{\theta}_{21}\theta_{,1} + \widehat{D}^{\psi}_{21}\psi_{,1}\right) + \widehat{A}^{kw}_{12}e_{,11} + \widehat{B}^{kw}_{12}k_{,11} + \widehat{C}^{kw}_{12}k^{\psi}_{,11} + \widehat{D}^{kw}_{21}w^{(0)}_{,11} + \widehat{D}^{kw}_{22}w^{(1)}_{,11} + \widehat{D}^{kw}_{23}w^{(2)}_{,11} \tag{C.2}$$

$$\widehat{Q}^{w2} = -\left(\widehat{D}^{w}_{31}w^{(0)}_{,11} + \widehat{D}^{w}_{32}w^{(1)}_{,11} + \widehat{D}^{w}_{33}w^{(2)}_{,11} + \widehat{D}^{\theta}_{31}\theta_{,1} + \widehat{D}^{\psi}_{31}\psi_{,1}\right) + \widehat{A}^{kw}_{13}e_{,11} + \widehat{B}^{kw}_{13}k_{,11} + \widehat{C}^{kw}_{13}k^{\psi}_{,11} + \widehat{D}^{kw}_{31}w^{(0)}_{,11} + \widehat{D}^{kw}_{32}w^{(1)}_{,11} + \widehat{D}^{kw}_{33}w^{(2)}_{,11} \tag{C.3}$$

$$E^{HR} = \widehat{A}^{w}_{11}w^{(0)}_{,11} + \widehat{A}^{w}_{12}w^{(1)}_{,11} + \widehat{A}^{w}_{13}w^{(2)}_{,11} + \widehat{A}^{\theta}_{11}\theta_{,1} + \widehat{A}^{\psi}_{11}\psi_{,1} - \left(\widehat{A}^{e}_{11}e_{,11} + \widehat{A}^{k}_{11}k_{,11} + \widehat{A}^{k\psi}_{11}k^{\psi}_{,11} + \widehat{A}^{kw}_{11}w^{(0)}_{,11} + \widehat{A}^{kw}_{12}w^{(1)}_{,11} + \widehat{A}^{kw}_{13}w^{(2)}_{,11}\right) \tag{C.4}$$

$$K^{HR} = \widehat{B}^{w}_{11}w^{(0)}_{,11} + \widehat{B}^{w}_{12}w^{(1)}_{,11} + \widehat{B}^{w}_{13}w^{(2)}_{,11} + \widehat{B}^{\theta}_{11}\theta_{,1} + \widehat{B}^{\psi}_{11}\psi_{,1} - \left(\widehat{A}^{k}_{11}e_{,11} + \widehat{B}^{k}_{11}k_{,11} + \widehat{B}^{k\psi}_{11}k^{\psi}_{,11} + \widehat{B}^{kw}_{11}w^{(0)}_{,11} + \widehat{B}^{kw}_{12}w^{(1)}_{,11} + \widehat{B}^{kw}_{13}w^{(2)}_{,11}\right) \tag{C.5}$$

$$K^{HR}_{\psi} = \widehat{C}^{w}_{11}w^{(0)}_{,11} + \widehat{C}^{w}_{12}w^{(1)}_{,11} + \widehat{C}^{w}_{13}w^{(2)}_{,11} + \widehat{C}^{\theta}_{11}\theta_{,1} + \widehat{C}^{\psi}_{11}\psi_{,1} - \left(\widehat{A}^{k\psi}_{11}e_{,11} + \widehat{B}^{k\psi}_{11}k_{,11} + \widehat{C}^{k\psi}_{11}k^{\psi}_{,11} + \widehat{C}^{kw}_{11}w^{(0)}_{,11} + \widehat{C}^{kw}_{12}w^{(1)}_{,11} + \widehat{C}^{kw}_{13}w^{(2)}_{,11}\right) \tag{C.6}$$

Furthermore, the terms shown in the boundary condition expression, i.e. Eq. (21), can read:

$$
\begin{aligned}
\overline{E}^{e}{}_{HR} &= \widehat{\mathbf{A}}^{w}\partial\mathbf{w} + \widehat{A}^{\theta}\theta + \widehat{A}^{\psi}\psi - \left(\widehat{\mathbf{A}}^{p}\overline{\mathbf{q}}_{\mathbf{p}} + \widehat{A}^{e}e_{,1} + \widehat{A}^{k}k_{,1} + \widehat{\mathbf{A}}^{k\psi}k^{\psi}_{,1} + \widehat{\mathbf{A}}^{kw}\partial\mathbf{w} + \widehat{\mathbf{A}}^{q}\partial\overline{\mathbf{q}}_{z}\right) \\
\overline{K}^{k}{}_{HR} &= \widehat{\mathbf{B}}^{w}\partial\mathbf{w} + \widehat{B}^{\theta}\theta + \widehat{B}^{\psi}\psi - \left(\widehat{\mathbf{B}}^{p}\overline{\mathbf{q}}_{\mathbf{p}} + \widehat{B}^{e}e_{,1} + \widehat{B}^{k}k_{,1} + \widehat{B}^{k\psi}k^{\psi}_{,1} + \widehat{\mathbf{B}}^{kw}\partial\mathbf{w} + \widehat{\mathbf{B}}^{q}\partial\overline{\mathbf{q}}_{z}\right) \\
\overline{K}^{k\psi}{}_{HR} &= \widehat{\mathbf{C}}^{w}\partial\mathbf{w} + \widehat{C}^{\theta}\theta + \widehat{C}^{\psi}\psi - \left(\widehat{\mathbf{C}}^{p}\overline{\mathbf{q}}_{\mathbf{p}} + \widehat{C}^{e}e_{,1} + \widehat{C}^{k}k_{,1} + \widehat{C}^{k\psi}k^{\psi}_{,1} + \widehat{\mathbf{C}}^{kw}\partial\mathbf{w} + \widehat{\mathbf{C}}^{q}\partial\overline{\mathbf{q}}_{z}\right) \\
\overline{\mathbf{Q}}_{HR} &= \left\lfloor \overline{Q}^{w0}_{1}HR \quad \overline{Q}^{w1}_{1}HR \quad \overline{Q}^{w2}_{1}HR \right\rfloor = \widehat{\mathbf{D}}^{w}\partial\mathbf{w} + \widehat{\mathbf{D}}^{\theta}\theta + \widehat{\mathbf{D}}^{\psi}\psi - \left(\widehat{\mathbf{D}}^{p}\overline{\mathbf{q}}_{\mathbf{p}} + \widehat{\mathbf{A}}^{kw^T}e_{,1} + \widehat{\mathbf{B}}^{kw^T}k_{,1} + \widehat{\mathbf{C}}^{kw^T}k^{\psi}_{,1} + \widehat{\mathbf{D}}^{kw}\partial\mathbf{w} + \widehat{\mathbf{D}}^{q}\partial\overline{\mathbf{q}}_{z}\right)
\end{aligned}
\tag{C.7}
$$

Moreover,

$$
\begin{aligned}
&\widetilde{A} = \langle E^{(k)}_1 + R_{13}{}^{(k)}A^{u}_{\sigma}\rangle; \quad \widetilde{B} = \langle x_3E^{(k)}_1 + R_{13}{}^{(k)}A^{\theta}_{\sigma}\rangle; \; \widetilde{A}^{\phi} = \langle E^{(k)}_1\mu^{(k)} + R_{13}{}^{(k)}A^{\psi}_{\sigma}\rangle; \\
&\widetilde{\mathbf{A}}^{w} = \langle R_{13}{}^{(k)}\mathbf{A}^{w}_{\sigma}\rangle; \quad \widetilde{\mathbf{A}}^{qz} = \langle R_{13}{}^{(k)}\mathbf{A}^{q_z}_{\sigma}\rangle; \; \widetilde{\mathbf{B}}^{w} = \langle x_3R_{13}{}^{(k)}\mathbf{A}^{w}_{\sigma}\rangle; \quad \widetilde{\mathbf{B}}^{qz} = \langle x_3R_{13}{}^{(k)}\mathbf{A}^{q_z}_{\sigma}\rangle; \\
&\widetilde{C} = \langle x_3E^{(k)}_1 + x_3R_{13}{}^{(k)}A^{u}_{\sigma}\rangle; \quad \widetilde{D} = \langle x^2_3E^{(k)}_1 + x_3R_{13}{}^{(k)}A^{\theta}_{\sigma}\rangle; \; \widetilde{B}^{\phi} = \langle x_3E^{(k)}_1\mu^{(k)} + zR_{13}{}^{(k)}A^{\psi}_{\sigma}\rangle; \\
&\widetilde{E}^{\phi} = \langle \mu^{(k)}E^{(k)}_1 + \mu^{(k)}R_{13}{}^{(k)}A^{u}_{\sigma}\rangle; \quad \widetilde{F}^{\phi} = \langle x_3\mu^{(k)}E^{(k)}_1 + \mu^{(k)}R_{13}{}^{(k)}A^{\theta}_{\sigma}\rangle; \\
&\widetilde{G}^{\phi} = \langle \mu^{(k)}E^{(k)}_1\mu^{(k)} + \mu^{(k)}R_{13}{}^{(k)}A^{\psi}_{\sigma}\rangle; \; \widetilde{\mathbf{C}}^{w} = \langle \mu^{(k)}R_{13}{}^{(k)}\mathbf{A}^{w}_{\sigma}\rangle; \quad \widetilde{\mathbf{C}}^{qz} = \langle \mu^{(k)}R_{13}{}^{(k)}\mathbf{A}^{q_z}_{\sigma}\rangle \\
&\mathbf{A}^{Nz} = \langle \mathbf{H}^{z}_{,3}{}^{T}A^{u}_{\sigma}\rangle; \quad \mathbf{B}^{Nz} = \langle \mathbf{H}^{z}_{,3}{}^{T}A^{\theta}_{\sigma}\rangle; \quad \mathbf{C}^{Nz} = \langle \mathbf{H}^{z}_{,3}{}^{T}A^{\psi}_{\sigma}\rangle; \; \mathbf{D}^{Nz} = \langle \mathbf{H}^{z}_{,3}{}^{T}\mathbf{A}^{w}_{\sigma}\rangle; \quad \mathbf{E}^{Nz} = \langle \mathbf{H}^{z}_{,3}{}^{T}\mathbf{A}^{q_z}_{\sigma}\rangle; \\
&\widehat{\mathbf{P}}^{w} = \langle \mathbf{H}^{z}_{,3}{}^{T}\mathbf{Z}_{p}\rangle; \; \widehat{\mathbf{P}}^{\theta} = \langle \mathbf{Z}_{p}\rangle; \; \widehat{\mathbf{P}}^{\psi} = \langle \mu^{(k)}_{,3}\mathbf{Z}_{p}\rangle;
\end{aligned}
\tag{C.8}
$$

Remembering that $S_t^{(k)} = 1/G_{13}^{(k)}$, the remaining quantities are expressed as follows:

$$
\begin{aligned}
&\widehat{\mathbf{A}}^w = \langle \widehat{A^z}\mathbf{H}^z\rangle;\quad \widehat{A}^\theta = \langle \widehat{A^z}\rangle;\quad \widehat{A}^\psi = \langle \widehat{A^z}\mu_{,3}^{(k)}\rangle;\ \widehat{\mathbf{A}}^p = \langle \widehat{A^z}S_t^{(k)}\mathbf{Z}_p\rangle;\quad \widehat{A}^e = \langle \widehat{A^z}S_t^{(k)}\widehat{A^z}\rangle;\\
&\widehat{A}^k = \langle \widehat{A^z}S_t^{(k)}\widehat{B^z}\rangle;\quad \widehat{A}^{k\psi} = \langle \widehat{A^z}S_t^{(k)}\widehat{D^z}\rangle;\ \widehat{\mathbf{A}}^{kw} = \langle \widehat{A^z}S_t^{(k)}\widehat{\mathbf{E}^z}\rangle;\quad \widehat{\mathbf{A}}^q = \langle \widehat{A^z}S_t^{(k)}\widehat{\mathbf{F}^z}\rangle;\\
&\widehat{\mathbf{B}}^w = \langle \widehat{B^z}\mathbf{H}^z\rangle;\quad \widehat{B}^\theta = \langle \widehat{B^z}\rangle;\quad \widehat{B}^\psi = \langle \widehat{B^z}\mu_{,3}^{(k)}\rangle;\ \widehat{\mathbf{B}}^p = \langle \widehat{B^z}S_t^{(k)}\mathbf{Z}_p\rangle;\quad \widehat{B}^e = \widehat{A}^k = \langle \widehat{B^z}S_t^{(k)}\widehat{A^z}\rangle;\\
&\widehat{B}^k = \langle \widehat{B^z}S_t^{(k)}\widehat{B^z}\rangle;\quad \widehat{B}^{k\psi} = \langle \widehat{B^z}S_t^{(k)}\widehat{D^z}\rangle;\quad \widehat{\mathbf{B}}^{kw} = \langle \widehat{B^z}S_t^{(k)}\widehat{\mathbf{E}^z}\rangle;\quad \widehat{\mathbf{B}}^q = \langle \widehat{B^z}S_t^{(k)}\widehat{\mathbf{F}^z}\rangle;\\
&\widehat{\mathbf{C}}^w = \langle \widehat{D^z}\mathbf{H}^z\rangle;\quad \widehat{C}^\theta = \langle \widehat{D^z}\rangle;\quad \widehat{C}^\psi = \langle \widehat{D^z}\mu_{,3}^{(k)}\rangle;\quad \widehat{\mathbf{C}}^p = \langle \widehat{D^z}S_t^{(k)}\mathbf{Z}_p\rangle;\quad \widehat{C}^e = \widehat{A}^{k\psi} = \langle \widehat{D^z}S_t^{(k)}\widehat{A^z}\rangle;\\
&\widehat{C}^k = \widehat{B}^{k\psi} = \langle \widehat{D^z}S_t^{(k)}\widehat{B^z}\rangle;\quad \widehat{C}^{k\psi} = \langle \widehat{D^z}S_t^{(k)}\widehat{D^z}\rangle;\quad \widehat{\mathbf{C}}^{kw} = \langle \widehat{D^z}S_t^{(k)}\widehat{\mathbf{E}^z}\rangle;\quad \widehat{\mathbf{C}}^q = \langle \widehat{D^z}S_t^{(k)}\widehat{\mathbf{F}^z}\rangle;\\
&\widehat{\mathbf{D}}^w = \langle \widehat{\mathbf{E}^z}^T\mathbf{H}^z\rangle;\ \widehat{\mathbf{D}}^\theta = \langle \widehat{\mathbf{E}^z}^T\rangle;\quad \widehat{\mathbf{D}}^\psi = \langle \widehat{\mathbf{E}^z}^T\mu_{,3}^{(k)}\rangle;\ \widehat{\mathbf{D}}^p = \langle \widehat{\mathbf{E}^z}^T S_t^{(k)}\mathbf{Z}_p\rangle;\ \widehat{\mathbf{D}}^e = \widehat{\mathbf{A}}^{kw^T} = \langle \widehat{\mathbf{E}^z}^T S_t^{(k)}\widehat{A^z}\rangle;\\
&\widehat{\mathbf{D}}^k = \widehat{\mathbf{B}}^{kw^T} = \langle \widehat{\mathbf{E}^z}^T S_t^{(k)}\widehat{B^z}\rangle;\quad \widehat{\mathbf{D}}^{k\psi} = \widehat{\mathbf{C}}^{kw^T} = \langle \widehat{\mathbf{E}^z}^T S_t^{(k)}\widehat{D^z}\rangle;\quad \widehat{\mathbf{D}}^{kw} = \langle \widehat{\mathbf{E}^z}^T S_t^{(k)}\widehat{\mathbf{E}^z}\rangle;\quad \widehat{\mathbf{D}}^q = \langle \widehat{\mathbf{E}^z}^T S_t^{(k)}\widehat{\mathbf{F}^z}\rangle;\\
&\widehat{\mathbf{E}}^w = \langle \mathbf{H}^{z^T}\widehat{\mathbf{F}^z}\rangle;\quad \widehat{\mathbf{E}}^\theta = \langle \widehat{\mathbf{F}^z}\rangle;\quad \widehat{\mathbf{E}}^\psi = \langle \mu_{,3}^{(k)}\widehat{\mathbf{F}^z}\rangle
\end{aligned}
\tag{C.9}
$$

Appendix D. – Full expressions of elemental stiffness matrix and load vector

In this appendix, the full expressions of the elemental stiffness matrix and load vector that appear in Eq. (36) are reported.

$$
\mathbf{K}_{dd}^{(e)} = \int_{L^{(e)}} \begin{bmatrix}
\left(\mathbf{L}_{,1}^T\widetilde{A}\mathbf{L}_{,1} + bh/\eta\,\mathbf{L}_{,1}^T\mathbf{L}_{,1}\right) & \mathbf{L}_{,1}^T\widetilde{\mathbf{A}}^w\mathbf{L}^w & \mathbf{L}_{,1}^T\widetilde{B}\mathbf{L}_{,1} & \mathbf{L}_{,1}^T\widetilde{A}^\phi\mathbf{L}_{,1}\\
\mathbf{L}^{wT}\mathbf{A}^{Nz}\mathbf{L}_{,1} & \left(\mathbf{L}^{wT}\mathbf{D}^{Nz}\mathbf{L}^w + \mathbf{L}_{,1}^{wT}\widehat{\mathbf{D}}^{wT}\mathbf{L}_{,1}^w + \right.\\ \left. + \mathbf{L}_{,1}^{wT}\widehat{\mathbf{D}}^w\mathbf{L}_{,1}^w - \mathbf{L}_{,1}^{wT}\widehat{\mathbf{D}}^{kw}\mathbf{L}_{,1}^w\right) & \left(\mathbf{L}^{wT}\mathbf{B}^{Nz}\mathbf{L}_{,1} + \right.\\ \left. + \mathbf{L}_{,1}^{wT}\widehat{\mathbf{D}}^\theta\mathbf{L}\right) & \left(\mathbf{L}^{wT}\mathbf{C}^{Nz}\mathbf{L}_{,1} + \right.\\ \left. + \mathbf{L}_{,1}^{wT}\widehat{\mathbf{D}}^\psi\mathbf{L}\right)\\
\mathbf{L}_{,1}^T\widetilde{C}\mathbf{L}_{,1} & \mathbf{L}^T\widehat{\mathbf{D}}^{\theta T}\mathbf{L}_{,1}^w + \mathbf{L}_{,1}^T\widetilde{\mathbf{B}}^w\mathbf{L}^w & \left(\mathbf{L}_{,1}^T\widetilde{D}\mathbf{L}_{,1} + \right.\\ \left. + bh/\eta\,\mathbf{L}_{,1}^T\mathbf{L}_{,1}\right) & \mathbf{L}_{,1}^T\widetilde{B}^\phi\mathbf{L}_{,1}\\
\mathbf{L}_{,1}^T\widetilde{E}^\phi\mathbf{L}_{,1} & \mathbf{L}^T\widehat{\mathbf{D}}^{\psi T}\mathbf{L}_{,1}^w + \mathbf{L}_{,1}^T\widetilde{\mathbf{C}}^w\mathbf{L}^w & \mathbf{L}_{,1}^T\widetilde{F}^\phi\mathbf{L}_{,1} & \left(\mathbf{L}_{,1}^T\widetilde{G}^\phi\mathbf{L}_{,1} + \right.\\ & & & \left. + bh/\eta\,\mathbf{L}_{,1}^T\mathbf{L}_{,1}\right)
\end{bmatrix} dx_1
\tag{D.1}
$$

$$
\mathbf{K}_{de}^{(e)} = \mathbf{K}_{ed}^{(e)^T} = \int_{L^{(e)}} \begin{bmatrix}
-bh/\eta\,\mathbf{L}_{,1}^T\mathbf{L} & \mathbf{0} & \mathbf{0}\\
\left(\mathbf{L}_{,1}^{wT}\widehat{\mathbf{A}}^{wT}\mathbf{L}_{,1} + \right. & \left(\mathbf{L}_{,1}^{wT}\widehat{\mathbf{B}}^{wT}\mathbf{L}_{,1} + \right. & \left(\mathbf{L}_{,1}^{wT}\widehat{\mathbf{C}}^{wT}\mathbf{L}_{,1} + \right.\\ \left. - \mathbf{L}_{,1}^{wT}\widehat{\mathbf{D}}^e\mathbf{L}_{,1}\right) & \left. - \mathbf{L}_{,1}^{wT}\widehat{\mathbf{D}}^k\mathbf{L}_{,1}\right) & \left. - \mathbf{L}_{,1}^{wT}\widehat{\mathbf{D}}^{k\psi}\mathbf{L}_{,1}\right)\\
\mathbf{L}^T\widehat{A}^\theta\mathbf{L}_{,1} & \left(\mathbf{L}^T\widehat{B}^\theta\mathbf{L}_{,1} + \right. & \mathbf{L}^T\widehat{C}^\theta\mathbf{L}_{,1}\\ & \left. - bh/\eta\,\mathbf{L}_{,1}^T\mathbf{L}\right) & \\
\mathbf{L}^T\widehat{A}^\psi\mathbf{L}_{,1} & \mathbf{L}^T\widehat{B}^\psi\mathbf{L}_{,1} & \left(\mathbf{L}^T\widehat{C}^\psi\mathbf{L}_{,1} + \right.\\ & & \left. - bh/\eta\,\mathbf{L}_{,1}^T\mathbf{L}\right)
\end{bmatrix} dx_1
\tag{D.2}
$$

$$
\mathbf{K}_{ee}^{(e)} = \int_{L^{(e)}} \begin{bmatrix}
-\mathbf{L}_{,1}^T\widehat{A}^e\mathbf{L}_{,1} + bh/\eta\,\mathbf{L}^T\mathbf{L} & -\mathbf{L}_{,1}^T\widehat{A}^k\mathbf{L}_{,1} & -\mathbf{L}_{,1}^T\widehat{A}^{k\psi}\mathbf{L}_{,1}\\
-\mathbf{L}_{,1}^T\widehat{B}^e\mathbf{L}_{,1} & -\mathbf{L}_{,1}^T\widehat{B}^k\mathbf{L}_{,1} + bh/\eta\,\mathbf{L}^T\mathbf{L} & -\mathbf{L}_{,1}^T\widehat{B}^{k\psi}\mathbf{L}_{,1}\\
-\mathbf{L}_{,1}^T\widehat{C}^e\mathbf{L}_{,1} & -\mathbf{L}_{,1}^T\widehat{C}^k\mathbf{L}_{,1} & -\mathbf{L}_{,1}^T\widehat{C}^{k\psi}\mathbf{L}_{,1} + bh/\eta\,\mathbf{L}^T\mathbf{L}
\end{bmatrix} dx_1
\tag{D.3}
$$

$$\mathbf{F}_d^{(e)} = \int_{L^{(e)}} \begin{Bmatrix} -\mathbf{L}_{,1}{}^T \widetilde{\mathbf{A}}^{qz} \overline{\mathbf{q}}_z + \mathbf{L}^T \overline{p}_1 \\ \mathbf{L}^T \overline{\mathbf{q}}_{Z_{ris}} + \mathbf{L}_{,1}^{w\,T} \widehat{\mathbf{D}}^q \partial \overline{\mathbf{q}}_z - \mathbf{L}^{w\,T} \mathbf{E}^{Nz} \overline{\mathbf{q}}_z - \mathbf{L}_{,1}^{w\,T} \widehat{\mathbf{E}}^w \partial \overline{\mathbf{q}}_z + \mathbf{L}_{,1}^{w\,T} \widehat{\mathbf{D}}^p \overline{\mathbf{q}}_\mathbf{p} - \mathbf{L}_{,1}^{w\,T} \widehat{\mathbf{P}}^w \overline{\mathbf{q}}_\mathbf{p} \\ -\mathbf{L}_{,1}{}^T \widetilde{\mathbf{B}}^{qz} \overline{\mathbf{q}}_z - \mathbf{L}^T \widehat{\mathbf{E}}^\theta \partial \overline{\mathbf{q}}_z + \mathbf{L}^T \overline{m}_1 - \mathbf{L}^T \widehat{\mathbf{P}}^\theta \overline{\mathbf{q}}_\mathbf{p} \\ -\mathbf{L}_{,1}{}^T \widetilde{\mathbf{C}}^{qz} \overline{\mathbf{q}}_z - \mathbf{L}^T \widehat{\mathbf{E}}^\psi \partial \overline{\mathbf{q}}_z - \mathbf{L}^T \widehat{\mathbf{P}}^\psi \overline{\mathbf{q}}_\mathbf{p} \end{Bmatrix} dx_1 \tag{D.4}$$

$$\mathbf{F}_s^{(e)} = \int_{L^{(e)}} \begin{Bmatrix} \mathbf{L}_{,1}{}^T \widehat{\mathbf{A}}^q \partial \overline{\mathbf{q}}_z + \mathbf{L}_{,1}{}^T \widehat{\mathbf{A}}^p \overline{\mathbf{q}}_\mathbf{p} \\ \mathbf{L}_{,1}{}^T \widehat{\mathbf{B}}^q \partial \overline{\mathbf{q}}_z + \mathbf{L}_{,1}{}^T \widehat{\mathbf{B}}^p \overline{\mathbf{q}}_\mathbf{p} \\ \mathbf{L}_{,1}{}^T \widehat{\mathbf{C}}^q \partial \overline{\mathbf{q}}_z + \mathbf{L}_{,1}{}^T \widehat{\mathbf{C}}^p \overline{\mathbf{q}}_\mathbf{p} \end{Bmatrix} dx_1 \tag{D.5}$$

with $\overline{\mathbf{q}}_{Z_{ris}}{}^T = \begin{bmatrix} \overline{q}_3 & \dfrac{h}{2}(\overline{p}_{3(T)} - \overline{p}_{3(B)}) & \dfrac{h^2}{4}\overline{q}_3 \end{bmatrix}$.

References

[1] S.K. Sahu, P.S.R. Sreekanth, S.V.K. Reddy, A brief review on advanced sandwich structures with customized design core and composite face sheet, Polymers 14 (2022) 4267, https://doi.org/10.3390/polym14204267.

[2] L.A. Carlsson, G.A. Kardomateas, Structural and Failure Mechanics of Sandwich Composites, first ed., Springer Dordrecht, Heidelberg London New York, 2011.

[3] N.J. Pagano, Exact solutions for composite laminates in cylindrical bending, J. Compos. Mater. 3 (1969) 398–411, https://doi.org/10.1177/002199836900300304.

[4] N.J. Pagano, Exact solutions for rectangular bidirectional composites and sandwich plates, J. Compos. Mater. 4 (1970) 20–34, https://doi.org/10.1177/002199837000400102.

[5] W.S. Burton, A.K. Noor, Three-dimensional solutions for thermomechanical stresses in sandwich panels and shells, J. Eng. Mech. 120 (1994) 2044–2071, https://doi.org/10.1061/(ASCE)0733-9399(1994)120:10, 2044.

[6] S. Brischetto, An exact 3d solution for free vibrations of multilayered cross-ply composite and sandwich plates and shells, Int. J. Appl. Mechanics 6 (2014) 1450076, https://doi.org/10.1142/S1758825114500768.

[7] J. Hohe and, W. Becker, Effective stress-strain relations for two-dimensional cellular sandwich cores: homogenization, material models, and properties, Appl. Mech. Rev. 55 (2001) 61–87, https://doi.org/10.1115/1.1425394.

[8] B. Lascoup, Z. Aboura, K. Khellil, M. Benzeggagh, Homogenization of the core layer in stitched sandwich structures, Compos. Sci. Technol. 70 (2010) 350–355, https://doi.org/10.1016/j.compscitech.2009.11.006.

[9] A. Catapano, M. Montemurro, A multi-scale approach for the optimum design of sandwich plates with honeycomb core. Part I: homogenisation of core properties, Compos. Struct. 118 (2014) 664–676, https://doi.org/10.1016/j.compstruct.2014.07.057.

[10] X. Martinez, J. Pons-Prats, F. Turon, M. Coma, L.G. Barbu, G. Bugeda, Multi-objective multi-scale optimization of composite structures, application to an aircraft overhead locker made with bio-composites, Mathematics 11 (2023) 165, https://doi.org/10.3390/math11010165.

[11] Y. Frostig, M. Baruch, O. Vilnay, I. Sheinman, High-order theory for sandwich-beam behavior with transversely flexible core, J. Eng. Mech. 118 (1992) 1026–1043, https://doi.org/10.1061/(ASCE)0733-9399(1992)118:5(1026.

[12] Y. Frostig, O.T. Thomsen, High-order free vibration of sandwich panels with a flexible core, Int. J. Solid Struct. 41 (2004) 1697–1724, https://doi.org/10.1016/j.ijsolstr.2003.09.051.

[13] V. Birman, G.A. Kardomateas, Review of current trends in research and applications of sandwich structures, Compos. B Eng. 142 (2018) 221–240, https://doi.org/10.1016/j.compositesb.2018.01.027.

[14] M. Di Sciuva, Bending, vibration and buckling of simply supported thick multilayered orthotropic plates: an evaluation of a new displacement model, J. Sound Vib. 105 (1986) 425–442, https://doi.org/10.1016/0022-460X(86)90169-0.

[15] M. Cho, R.R. Parmerter, An efficient higher-order plate theory for laminated composites, Compos. Struct. 20 (1992) 113–123, https://doi.org/10.1016/0263-8223(92)90067-M.

[16] A. Loredo, M. D'Ottavio, P. Vidal, O. Polit, A family of higher-order single layer plate models meeting Cz0-requirements for arbitrary laminates, Compos. Struct. 225 (2019) 111146, https://doi.org/10.1016/j.compstruct.2019.111146.

[17] U. Icardi, A. Urraci, Free and forced vibration of laminated and sandwich plates by zig-zag theories differently accounting for transverse shear and normal deformability, Aerospace 5 (2018) 108, https://doi.org/10.3390/aerospace5040108.

[18] A. Tessler, M. Di Sciuva, M. Gherlone, Refinement of Timoshenko beam theory for composite and sandwich beams using zigzag kinematics, NASA/TP-2007-215086 (2007) 1–45.

[19] L. Iurlaro, M. Gherlone, M. Mattone, M. Di Sciuva, Experimental assessment of the Refined Zigzag Theory for the static bending analysis of sandwich beams, Jnl of Sandwich Structures & Materials 20 (2018) 86–105, https://doi.org/10.1177/1099636216650614.

[20] L. Iurlaro, A. Ascione, M. Gherlone, M. Mattone, M. Di Sciuva, Free vibration analysis of sandwich beams using the Refined Zigzag Theory: an experimental assessment, Meccanica 50 (2015) 2525–2535, https://doi.org/10.1007/s11012-015-0166-4.

[21] K.A. Hasim, Isogeometric static analysis of laminated composite plane beams by using refined zigzag theory, Compos. Struct. 186 (2018) 365–374, https://doi.org/10.1016/j.compstruct.2017.12.033.

[22] K.A. Hasim, A. Kefal, E. Madenci, Isogeometric plate element for unstiffened and blade stiffened laminates based on refined zigzag theory, Compos. Struct. 222 (2019) 110931, https://doi.org/10.1016/j.compstruct.2019.110931.

[23] K.A. Hasim, A. Kefal, Isogeometric static analysis of laminated plates with curvilinear fibers based on Refined Zigzag Theory, Compos. Struct. 256 (2021) 113097, https://doi.org/10.1016/j.compstruct.2020.113097.

[24] R.M. Groh, P.M. Weaver, A. Tessler, Application of the Refined Zigzag Theory to the Modeling of Delaminations in Laminated Composites, 2015, pp. 1–22. NASA/TM-2015-218808.

[25] A. Eijo, E. Oñate, S. Oller, A numerical model of delamination in composite laminated beams using the LRZ beam element based on the refined zigzag theory, Compos. Struct. 104 (2013) 270–280, https://doi.org/10.1016/j.compstruct.2013.04.035.

[26] I.E. Tabrizi, A. Kefal, J.S.M. Zanjani, C. Akalin, M. Yildiz, Experimental and numerical investigation on fracture behavior of glass/carbon fiber hybrid composites using acoustic emission method and refined zigzag theory, Compos. Struct. 223 (2019) 110971, https://doi.org/10.1016/j.compstruct.2019.110971.

[27] M. Ermis, M. Dorduncu, A. Kutlu, Peridynamic differential operator for stress analysis of imperfect functionally graded porous sandwich beams based on refined zigzag theory, Appl. Math. Model. (2024), https://doi.org/10.1016/j.apm.2024.05.032.

[28] V.-H. Truong, Q.-H. Le, J. Lee, J.-W. Han, A. Tessler, S.-N. Nguyen, An efficient neural network approach for laminated composite plates using refined zigzag theory, Compos. Struct. 348 (2024) 118476, https://doi.org/10.1016/j.compstruct.2024.118476.
[29] P. Cerracchio, M. Gherlone, M. Di Sciuva, A. Tessler, A novel approach for displacement and stress monitoring of sandwich structures based on the inverse Finite Element Method, Compos. Struct. 127 (2015) 69–76, https://doi.org/10.1016/j.compstruct.2015.02.081.
[30] A. Kefal, I.E. Tabrizi, M. Yildiz, A. Tessler, A smoothed iFEM approach for efficient shape-sensing applications: numerical and experimental validation on composite structures, Mech. Syst. Signal Process. 152 (2021) 107486, https://doi.org/10.1016/j.ymssp.2020.107486.
[31] F. Ganjdoust, A. Kefal, A. Tessler, A novel delamination damage detection strategy based on inverse finite element method for structural health monitoring of composite structures, Mech. Syst. Signal Process. 192 (2023) 110202, https://doi.org/10.1016/j.ymssp.2023.110202.
[32] M. Dorduncu, A. Kutlu, E. Madenci, Triangular C0 continuous finite elements based on refined zigzag theory {2,2} for free and forced vibration analyses of laminated plates, Compos. Struct. 281 (2022) 115058, https://doi.org/10.1016/j.compstruct.2021.115058.
[33] B. Yurtsever, Y. Bab, A. Kutlu, M. Dorduncu, A new C^0continuous refined zigzag {1,2} finite element formulation for flexural and free vibration analyses of laminated composite beams, Compos. Struct. 331 (2024) 117890, https://doi.org/10.1016/j.compstruct.2024.117890.
[34] A. Barut, E. Madenci, A. Tessler, C0-continuous triangular plate element for laminated composite and sandwich plates using the {2,2} – refined Zigzag Theory, Compos. Struct. 106 (2013) 835–853, https://doi.org/10.1016/j.compstruct.2013.07.024.
[35] L. Iurlaro, M. Gherlone, M. Di Sciuva, The (3,2)-Mixed Refined Zigzag Theory for generally laminated beams: theoretical development and C^0 finite element formulation, Int. J. Solid Struct. (2015) 73–74, https://doi.org/10.1016/j.ijsolstr.2015.07.028, 1–19.
[36] R.M.J. Groh, P.M. Weaver, A computationally efficient 2D model for inherently equilibrated 3D stress predictions in heterogeneous laminated plates. Part I: model formulation, Compos. Struct. 156 (2016) 171–185, https://doi.org/10.1016/j.compstruct.2015.11.078.
[37] R.M.J. Groh, P.M. Weaver, A computationally efficient 2D model for inherently equilibrated 3D stress predictions in heterogeneous laminated plates. Part II: model validation, Compos. Struct. 156 (2016) 186–217, https://doi.org/10.1016/j.compstruct.2015.11.077.
[38] A. Kutlu, M. Dorduncu, T. Rabczuk, A novel mixed finite element formulation based on the refined zigzag theory for the stress analysis of laminated composite plates, Compos. Struct. 267 (2021) 113886, https://doi.org/10.1016/j.compstruct.2021.113886.
[39] M. Sorrenti, M. Di Sciuva, An enhancement of the warping shear functions of refined zigzag theory, J. Appl. Mech. 88 (2021), https://doi.org/10.1115/1.4050908.
[40] M. Sorrenti, M. Gherlone, M. Di Sciuva, Buckling analysis of angle-ply multilayered and sandwich plates using the enhanced Refined Zigzag Theory, PEAS 71 (2022) 84, https://doi.org/10.3176/proc.2022.1.08.
[41] M. Sorrenti, M. Gherlone, Dynamic analysis of sandwich beams with adhesive layers using the mixed refined zigzag theory, in: Proceedings of the International Conference on Numerical Analysis and Applied Mathematics 2021 (ICNAAM-2021), AIP Publishing, Rhodes, Greece, 2023, p. 4, https://doi.org/10.1063/5.0162539.
[42] M. Sorrenti, M. Gherlone, A new mixed model based on the enhanced-Refined Zigzag Theory for the analysis of thick multilayered composite plates, Compos. Struct. 311 (2023) 116787, https://doi.org/10.1016/j.compstruct.2023.116787.
[43] L.L. Yan, B. Han, B. Yu, C.Q. Chen, Q.C. Zhang, T.J. Lu, Three-point bending of sandwich beams with aluminum foam-filled corrugated cores, Mater. Des. 60 (2014) 510–519, https://doi.org/10.1016/j.matdes.2014.04.014.
[44] A. Ascione, A.C. Orifici, M. Gherlone, Experimental and numerical investigation of the refined zigzag theory for accurate buckling analysis of highly heterogeneous sandwich beams, Int. J. Str. Stab. Dyn. 20 (2020) 2050078, https://doi.org/10.1142/S0219455420500789.
[45] Ł. Pyrzowski, B. Sobczyk, Local and global response of sandwich beams made of GFRP facings and PET foam core in three point bending test, Compos. Struct. 241 (2020) 112122, https://doi.org/10.1016/j.compstruct.2020.112122.
[46] F. Xia, Y. Durandet, P.J. Tan, D. Ruan, Three-point bending performance of sandwich panels with various types of cores, Thin-Walled Struct. 179 (2022) 109723, https://doi.org/10.1016/j.tws.2022.109723.
[47] G. Sala, L. Di Landro, A. Airoldi, P. Bettini, Fibre optics health monitoring for aeronautical applications, Meccanica 50 (2015) 2547–2567, https://doi.org/10.1007/s11012-015-0200-6.
[48] M. Kulpa, T. Howiacki, A. Wiater, T. Siwowski, R. Sieńko, Strain and displacement measurement based on distributed fibre optic sensing (DFOS) system integrated with FRP composite sandwich panel, Measurement 175 (2021) 109099, https://doi.org/10.1016/j.measurement.2021.109099.
[49] A. Biondi, R. Wu, L. Cao, B. Gopalan, J. Ivey, C. Garces, M. Mitchell, J.D. Williams, X. Wang, Fiber optic sensing textile for strain monitoring in composite substrates, Sensors 22 (2022) 9262, https://doi.org/10.3390/s22239262.
[50] M. Di Sciuva, M. Gherlone, A global/local third-order Hermitian displacement field with damaged interfaces and transverse extensibility: analytical formulation, Compos. Struct. 59 (2003) 419–431, https://doi.org/10.1016/S0263-8223(02)00168-X.
[51] K. Washizu, Variational Methods in Elasticity and Plasticity, Second, Pergamon Press, 1975.
[52] I. Babuška, The finite element method with Lagrangian multipliers, Numer. Math. 20 (1973) 179–192, https://doi.org/10.1007/BF01436561.
[53] F. Brezzi, On the existence, uniqueness and approximation of saddle-point problems arising from Lagrangian multipliers, R.A.I.R.O. Analyse, Numérique 8 (1974) 129–151, https://doi.org/10.1051/m2an/197408R201291.
[54] A. Tessler, M. Di Sciuva, M. Gherlone, Refined Zigzag Theory for Laminated Composite and Sandwich Plates, 2009, pp. 1–53. NASA/TP-2009-215561.
[55] 3M Scotch-Weld Structural Adhesive Film AF, 3M Aerospace and Aircraft Maintenance Department, St. Paul, MN, 2009, 163-2.
[56] M. Sorrenti, Refined Zigzag Models for the Response of General Multilayered Composite and Sandwich Structures: Numerical and Experimental Investigations, PhD Thesis, 2023. Politecnico di Torino, https://iris.polito.it/handle/11583/2981462?mode=simple.
[57] Rohacell 31 IG-F PMI foam - easy composites. https://www.easycomposites.co.uk/Rohacell31-IG-F-PMI-Foam, 2022.
[58] P. Madabhusi-Raman, J.F. Davalos, Static shear correction factor for laminated rectangular beams, Compos. B Eng. 27 (1996) 285–293, https://doi.org/10.1016/1359-8368(95)00014-3.